

AD\_\_\_\_\_

Award Number: W81XWH-12-1-0307

TITLE: Investigating Ductal Carcinoma in Situ Using Noninvasive Imaging of Genetically Engineered Mouse Models

PRINCIPAL INVESTIGATOR: Dr. Sanaz Jansen

CONTRACTING ORGANIZATION: The Geneva Foundation  
Tacoma, WA 98402

REPORT DATE: August 2013

TYPE OF REPORT: Annual Summary

PREPARED FOR: U.S. Army Medical Research and Materiel Command  
Fort Detrick, Maryland 21702-5012

DISTRIBUTION STATEMENT: Approved for Public Release;  
Distribution Unlimited

The views, opinions and/or findings contained in this report are those of the author(s) and should not be construed as an official Department of the Army position, policy or decision unless so designated by other documentation.

<b>REPORT DOCUMENTATION PAGE</b>				<i>Form Approved</i> <i>OMB No. 0704-0188</i>	
Public reporting burden for this collection of information is estimated to average 1 hour per response, including the time for reviewing instructions, searching existing data sources, gathering and maintaining the data needed, and completing and reviewing this collection of information. Send comments regarding this burden estimate or any other aspect of this collection of information, including suggestions for reducing this burden to Department of Defense, Washington Headquarters Services, Directorate for Information Operations and Reports (0704-0188), 1215 Jefferson Davis Highway, Suite 1204, Arlington, VA 22202-4302. Respondents should be aware that notwithstanding any other provision of law, no person shall be subject to any penalty for failing to comply with a collection of information if it does not display a currently valid OMB control number. <b>PLEASE DO NOT RETURN YOUR FORM TO THE ABOVE ADDRESS.</b>					
<b>1. REPORT DATE</b> August 2013		<b>2. REPORT TYPE</b> Annual Summary		<b>3. DATES COVERED</b> 1 August 2012 – 31 July 2013	
<b>4. TITLE AND SUBTITLE</b>  Investigating Ductal Carcinoma in Situ Using Noninvasive Imaging of Genetically Engineered Mouse Models				<b>5a. CONTRACT NUMBER</b>	
				<b>5b. GRANT NUMBER</b> W81XWH-12-1-0307	
				<b>5c. PROGRAM ELEMENT NUMBER</b>	
<b>6. AUTHOR(S)</b>  Dr. Sanaz Jansen  <b>E-Mail:</b> cpfortmiller@genevausa.org				<b>5d. PROJECT NUMBER</b>	
				<b>5e. TASK NUMBER</b>	
				<b>5f. WORK UNIT NUMBER</b>	
<b>7. PERFORMING ORGANIZATION NAME(S) AND ADDRESS(ES)</b>  The Geneva Foundation Tacoma, WA 98402				<b>8. PERFORMING ORGANIZATION REPORT NUMBER</b>	
<b>9. SPONSORING / MONITORING AGENCY NAME(S) AND ADDRESS(ES)</b> U.S. Army Medical Research and Materiel Command Fort Detrick, Maryland 21702-5012				<b>10. SPONSOR/MONITOR'S ACRONYM(S)</b>	
				<b>11. SPONSOR/MONITOR'S REPORT NUMBER(S)</b>	
<b>12. DISTRIBUTION / AVAILABILITY STATEMENT</b> Approved for Public Release; Distribution Unlimited					
<b>13. SUPPLEMENTARY NOTES</b>					
<b>14. ABSTRACT</b>  Our main goal in this proposal was to investigate the capacity for quantitative in vivo MRI biomarkers to represent underlying molecular signatures of DCIS, using the preclinical genetically engineered mouse (GEM) model framework to our hypotheses. We focused three key molecular pathways—Rb, p53, BRAC1—and whether MRI signatures can identify these molecular subtypes of disease. This report describes our experience in the first six months executing the SOW. We soon discovered limitations in our original GEM modeling strategy suggesting that our proposed studies could not be effectively performed. We therefore designed an alternative GEM modeling strategy that successfully addressed these limitations. We also developed novel MRI techniques to detect, characterize and follow progression of the preinvasive malignancies in the mouse mammary gland at high spatial resolution, and high frequency (rapidly imaging every few days).					
<b>15. SUBJECT TERMS</b> Ductal carcinoma in situ, mouse models, magnetic resonance imaging, biomarkers, DCIS					
<b>16. SECURITY CLASSIFICATION OF:</b>			<b>17. LIMITATION OF ABSTRACT</b>  UU	<b>18. NUMBER OF PAGES</b>  56	<b>19a. NAME OF RESPONSIBLE PERSON</b> USAMRMC
<b>a. REPORT</b> U	<b>b. ABSTRACT</b> U	<b>c. THIS PAGE</b> U			<b>19b. TELEPHONE NUMBER</b> (include area code)

## Table of Contents

### Page

<b>Introduction.....</b>	<b>05</b>
<b>Body.....</b>	<b>11</b>
<b>Key Research Accomplishments.....</b>	<b>19</b>
<b>Reportable Outcomes.....</b>	<b>19</b>
<b>Conclusion.....</b>	<b>19</b>
<b>References.....</b>	<b>20</b>
<b>Appendices .....</b>	<b>20</b>

## INTRODUCTION

**Background:** Improvements in the early detection of breast cancer have yielded a major reduction in mortality because of the downward stage shifting of cancers at initial diagnosis: more women are diagnosed with stage I invasive ductal carcinoma (IDC) and the preinvasive ductal carcinoma *in situ* (DCIS) (Figure 1) now than before screening mammography was widely implemented. DCIS incidence in particular has skyrocketed, from comprising only ~2% of all breast cancers in the 1970's to ~20-30% now.

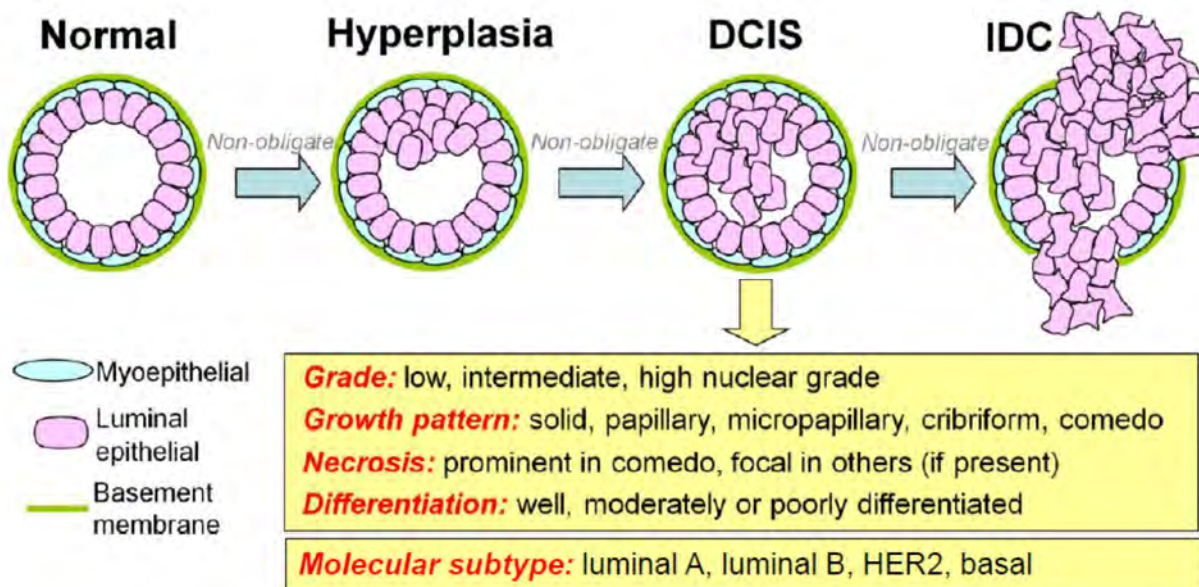


**Figure 1: The stages of breast cancer.** Within the normal mammary duct, an inner layer of luminal epithelial cells and a basal layer of myoepithelial cells are surrounded by a basement membrane. In benign hyperplasia, epithelial cells have proliferated within the duct while retaining a largely normal phenotype. In ductal carcinoma *in situ* (DCIS), the cells appear phenotypically different from normal epithelia — poorly differentiated DCIS more so than well differentiated DCIS — yet are still confined by the basement membrane. DCIS is classified into several subtypes based on its histopathological presentation, including grade, growth pattern and necrosis. Once the neoplastic cells invade beyond a degraded basement membrane into the surrounding breast stroma, they have transitioned to invasive ductal carcinoma (IDC).

Concomitant with these improvements in early detection has been a growing clinical concern that some patients with DCIS may be over-diagnosed and over-treated, as indirect evidence suggests that a significant portion of DCIS lesions may never progress to invasive carcinomas. Unfortunately, there is no way now to identify patients with indolent disease (Table 1). Thus, herein lays the clinical motivation for this proposal: to find prognostic biomarkers for DCIS so that indolent and aggressive cancers can be distinguished from one another (if possible), allowing for more tailored patient management.

Molecular Markers	Functions	Molecular signatures correlating with increased risk of progression
ER, PR	Steroid receptors	ER– HER2+
HER2	Regulates proliferation and apoptosis	ER–/HER2+ ER–/HER2+/Ki-67+
p53	Regulates cell-cycle, apoptosis and genomic stability; p53 is an important tumor suppressor	p53+
Rb/p16 pathway	Regulates cell-cycle; Rb is an important tumor suppressor	Cyclin D– p16+
Ki-67	Proliferation marker	Ki-67+ COX-2+
COX-2	Enzyme for prostaglandin synthesis; expressed during inflammatory response	p16+/COX-2-/Ki-67+ (DCIS recurrence) p16+/COX-2+/Ki-67+ (invasive recurrence)
Akt/PTEN pathway	Regulates proliferation, survival and motility; PTEN is an important tumor suppressor	
BRCA1/2	DNA damage repair	
c-myc	Transcription factor that can activate proliferation; c-myc is a proto-oncogene	
VEGF, vascular patterns	Angiogenesis and vascular markers	
cyclin A, cyclin E, p21, p27	Cell-cycle regulators	p21+
Bcl-2, Bax, Survivin	Apoptosis regulators	Bcl-2– Survivin+

**Table 1: Summary of the molecular markers that have been studied in human DCIS.** Included are the molecular signatures that have been shown to correlate (even weakly) with an increased risk of subsequent progression in some reports. Note that none of these molecular markers can be used to reliably distinguish indolent and aggressive DCIS. In this proposal, we focus on the p53, BRCA1 and Rb pathways (highlighted).

Our approach in this proposal is to investigate [biomarkers of DCIS](#) in a preclinical setting, by developing genetically engineered (GEM) models that develop preinvasive cancers analogous to human DCIS. We further focus on imaging biomarkers, specifically magnetic resonance imaging (MRI) features. Imaging biomarkers have the advantage over other molecular marker (DNA, RN or protein based) of being *in vivo* and noninvasive. However, they also have the disadvantage of not being directly representative of a molecular signature or pathway. Rather, they have the potential to be surrogate features of underlying molecular pathway aberrations. Therefore, our main goal in this proposal is to investigate the capacity for quantitative *in vivo* MRI features to represent underlying molecular signatures of DCIS, in the preclinical GEM model framework.

**Hypotheses:** We identified the following hypotheses to be investigated in the Statement of Work (SOW).

**Hypothesis #1. GEMs provide an experimental framework in which to improve the image-based characterization of molecular subtypes and prognosis of DCIS.** GEMs that use different molecular drivers of tumorigenesis have, in context of invasive breast cancer, yielded different molecular subtypes and aggressiveness of disease. Such models

are often used for the development of novel and advanced imaging techniques. We thus contend that a similar paradigm may be applicable for preinvasive cancers—that by using a diversity of molecular drivers it is possible to generate preinvasive neoplasias of different molecular subtypes, which can serve as an excellent test-bed for evaluation of improved imaging strategies.

**Hypothesis #2. Altering the pRb, p53 and BRCA1 pathways individually and in combination within the mammary epithelium will yield different molecular subtypes of preinvasive neoplasias.** We seek to establish and utilize GEMs of different molecular subtypes of DCIS in a homogeneous background. To achieve this, we have selected three drivers that have been shown to be highly relevant to subsets of human breast cancers (Figure 2): pRb, p53 and BRCA1. Aberrant activity of these pathways has also been implicated in studies focusing on DCIS (Figures 3 and 4, Table 2). To disrupt the p53 and BRCA1 pathways we will utilize existing conditional GEM models<sup>1</sup>. To achieve functional inactivation of pRb and family related proteins we have developed a strategy to dominantly interfere with pRb/p107/p130 via expression of the N-terminal SV40 T Ag domain (T<sub>121</sub>)<sup>2</sup>. Employing this strategy to functionally inactivate the pRb family proteins via expression of T<sub>121</sub> has been used successfully to generate highly penetrant mouse models of breast<sup>3,4</sup> and prostate adenocarcinoma<sup>5,6</sup>, and high grade astrocytoma<sup>7,8</sup>. Here we propose to target conditional expression of T<sub>121</sub> to the luminal, i.e., cytokeratin 18 (K18) positive, mammary epithelia by using the K18 promoter, which has the advantage of being hormone independent.

**Hypothesis #3. Different molecular subtypes of preinvasive neoplasias will exhibit significantly altered MR image-based characterization.** Dynamic contrast enhanced MRI (DCEMRI) is a widely used technique that provides both a morphologic and functional lesion characterization via analysis of contrast media uptake and washout—or kinetic—curves. The rate of contrast uptake and washout reflects the perfusion and diffusion of contrast media from blood vessels into the tumor. Quantitative kinetic parameters are in turn related to vascular properties, such as capillary permeability, surface area and blood flow<sup>9</sup>. In both human and murine studies, DCEMRI parameters of invasive breast cancer have been shown to correlate with tumor biology and even prognosis<sup>10,11</sup>. We therefore propose to test a similar hypothesis for preinvasive cancers.

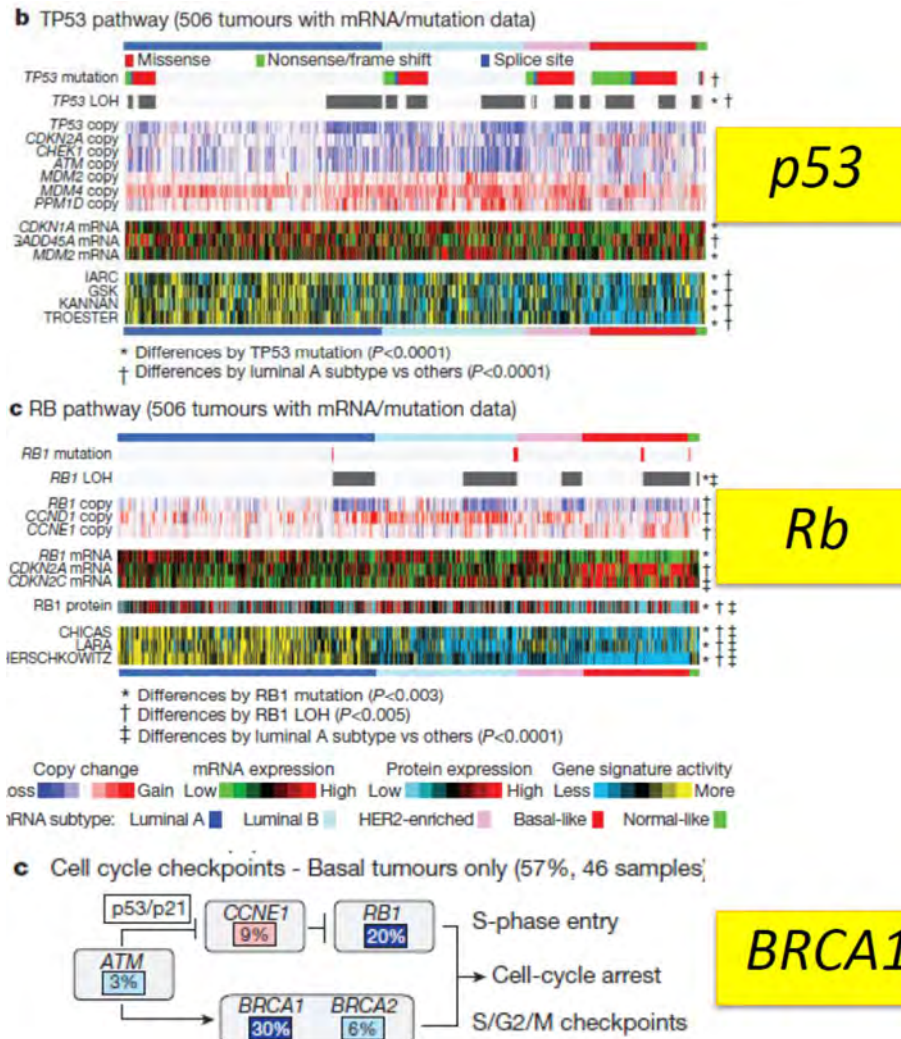


**Figure 2: p53, Rb and BRCA1 are key tumor suppressor pathways altered in breast cancer.** Based on figures from the recent report by the The Cancer Genome Atlas (TCGA) on breast cancer<sup>12</sup>.



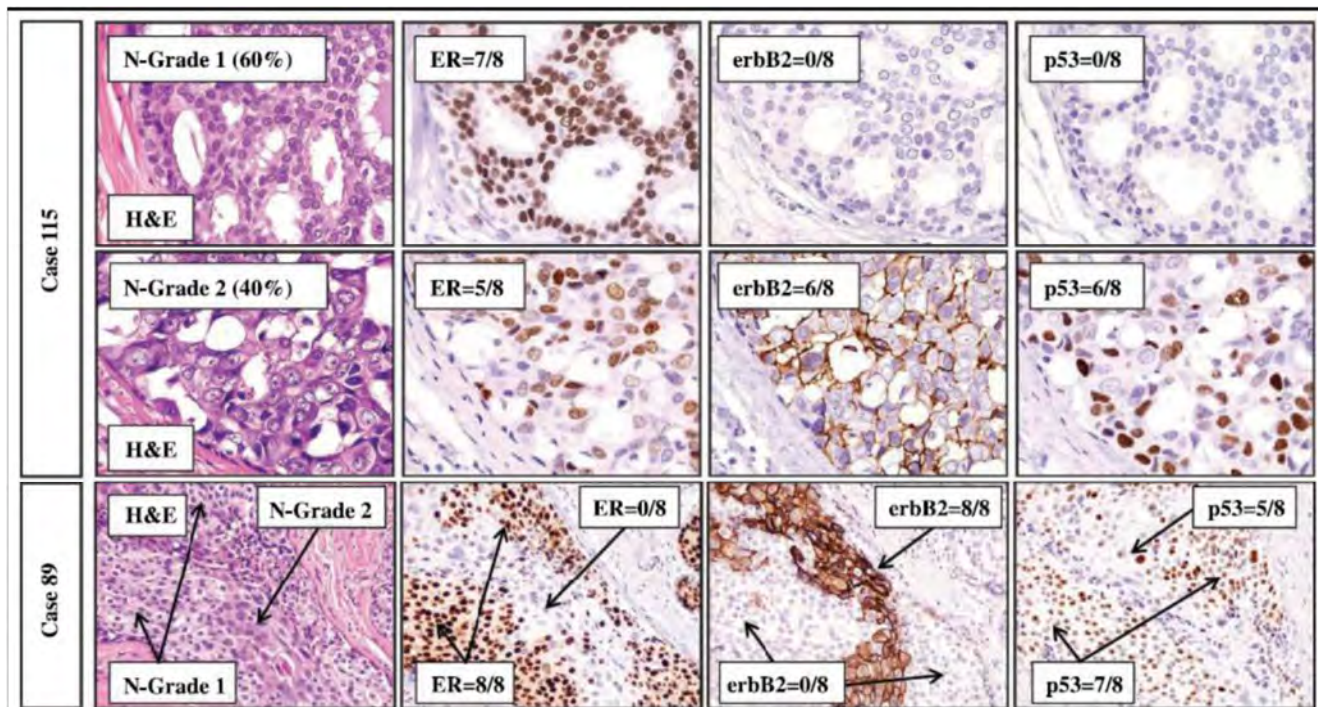


**Figure 3: Clinical evidence for the role of p53 in DCIS.** Figure from Allred et al<sup>13</sup> demonstrating that accumulation of p53 correlates with increased heterogeneity of DCIS.



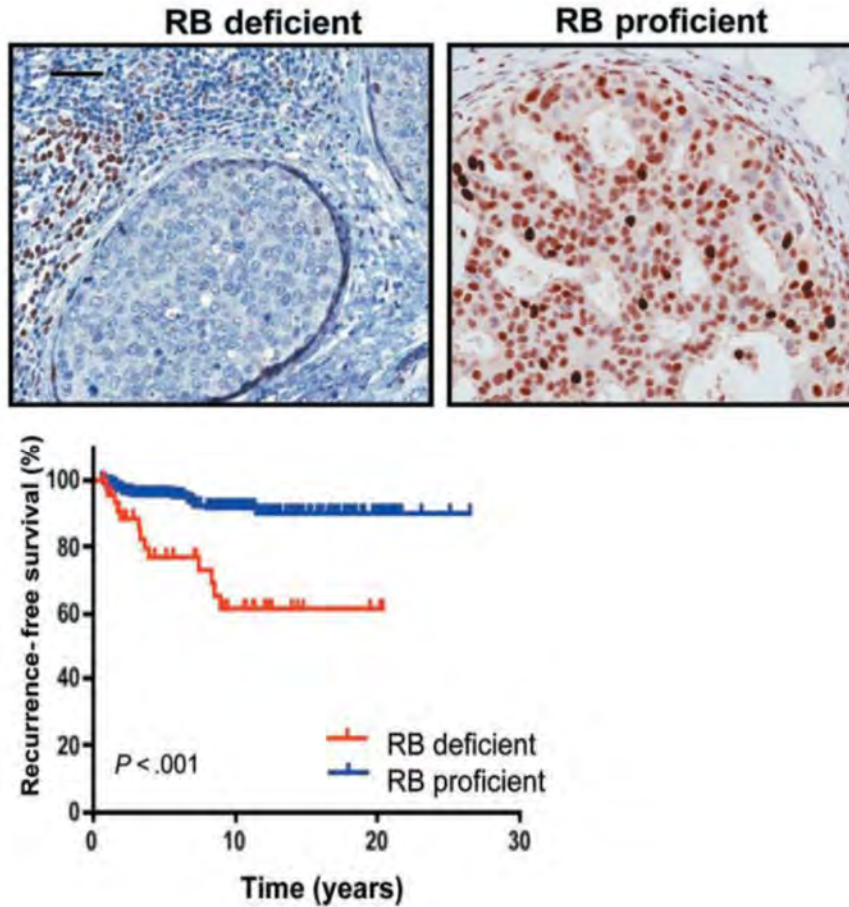


**Figure 4: Clinical evidence for role of Rb in DCIS.** Figures from Knudsen et al<sup>14</sup> demonstrating Increased recurrence in DCIS patients with Rb deficient lesions. In our proposal, we use expression of T<sub>121</sub> to functionally inactivate the Rb pathway in GEM models.

Screening trial, Mammo+MRI	No. of tumors in BRCA MC	No. tumors that are DCIS
Warner et al, 2011	9	0/9
Sardanelli et al, 2010	21	2/10
Rjinsburger et al, 2010	21	2/21
Gilbert et al, 2009	15	0/15
Shah et al, 2009	11	2/11
Kaas et al, 2008	39	3/39
Schrading et al, 2008	23	0/14
<b>Total</b>	<b>139</b>	<b>9/139 (6%)</b>

**Table 2: Clinical evidence for the role of BRCA1 in DCIS.** Compiling data from screening trials for breast cancer using MRI and mammography finds that only 6% of BRCA1 mutation carriers (MC) have DCIS, compared to 20-30% in the general population.



luminal epithelial cells. Conditional models of p53 and BRCA1 loss are also utilized. Focal induction is achieved in adult mice by using direct injection of lentiviral Cre recombinase.

However, early on during this reporting period we realized that there may be substantial flaws with our original GEM modeling strategy. There were two main problems. First, our more recent experience suggested the K18 promoter did not drive conditional T<sub>121</sub> expression strongly enough to successfully initiate tumorigenesis via Rb inactivation (Figure 6), even after widespread recombination achieved by crossing with the Wap-Cre mouse strain.

## WAP-Cre induction

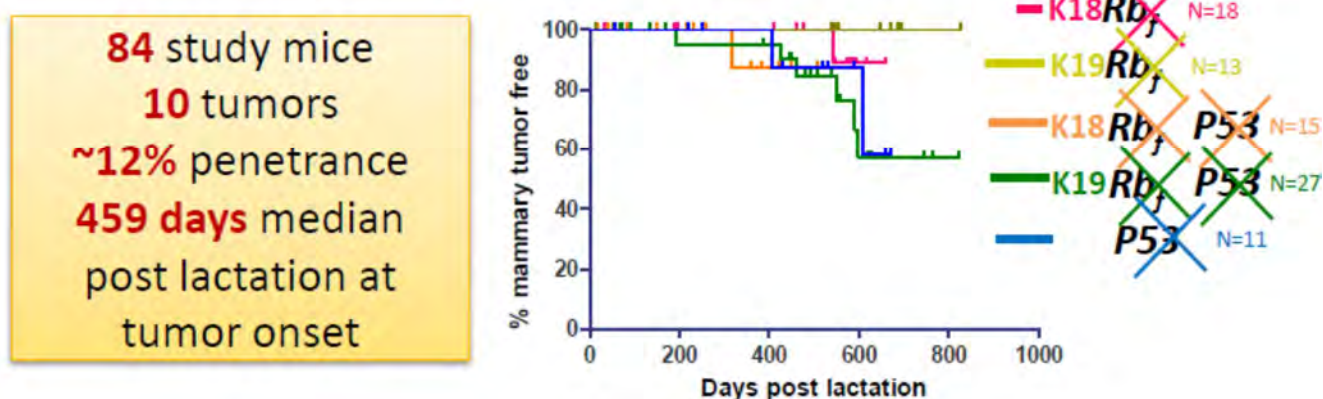


**Figure 6: K18 promoter driving expression of T121 does not reliably initiate tumorigenesis.** We crossed the K18-T121 model to the Wap-Cre mouse strain, to investigate efficiency of tumor initiation after widespread Cre expression. As shown in the pink line above, tumor incidence was very low in this model. We further crossed these mice onto the conditional model of p53 loss (orange line), which again demonstrates low tumor incidence and late onset.

Second, our recent *in vitro* and *in vivo* studies suggested that lentiviral-mediated Cre delivery was a very inefficient method for achieving recombination (see Task 1c below). Therefore, the weak initiating event (due to the K18 promoter) coupled with poor recombination efficiency (due to lentiviral delivery of Cre) combined to strongly indicate our original GEM modeling strategy would not yield penetrant mouse models of DCIS.

In light of these potential challenges, we proposed an [alternative GEM modeling strategy](#), illustrated in Figure 7 below. This new strategy was submitted to the DOD as a modification to our proposal (see Appendix A), and was approved.

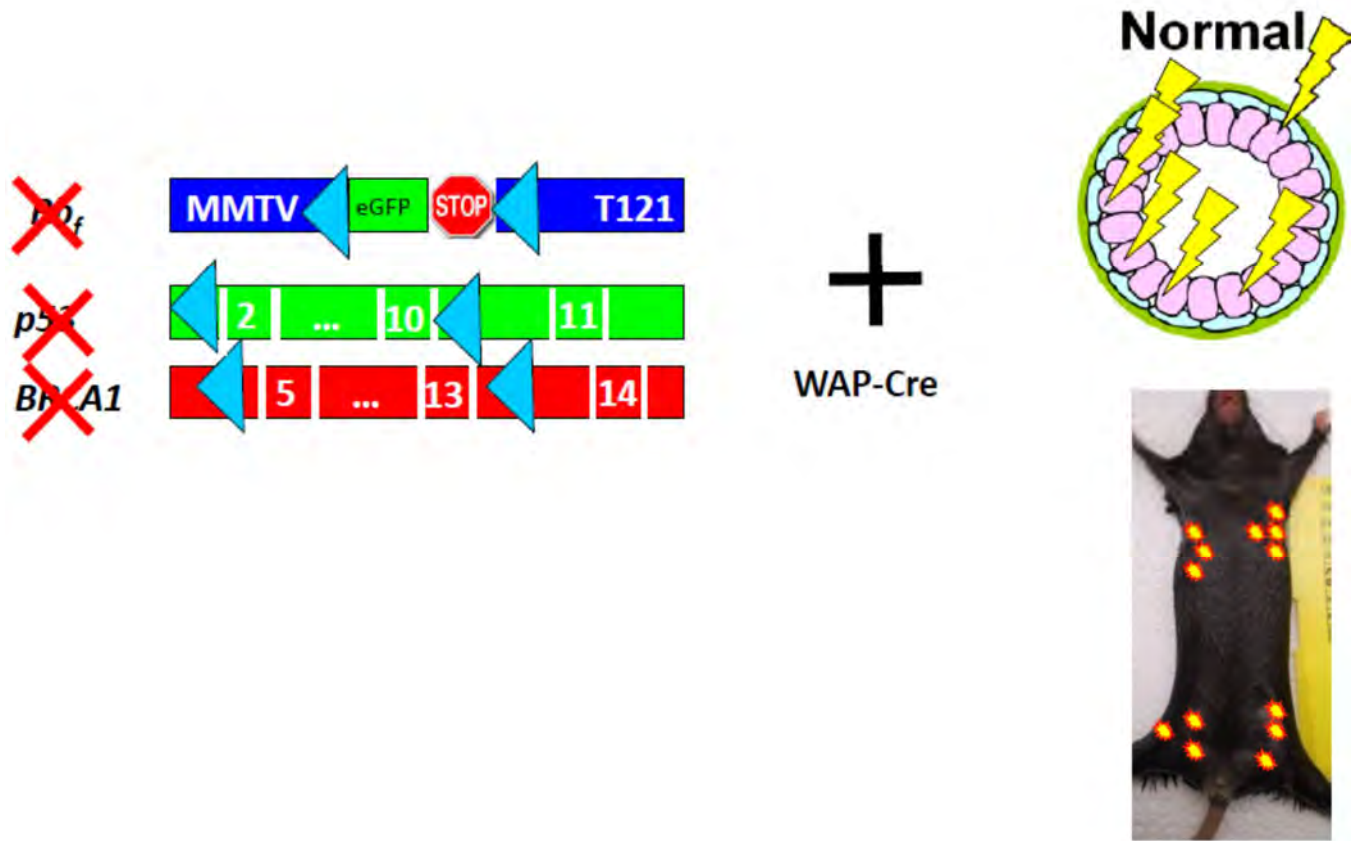


**Figure 7: Alternative GEM modeling strategy.** The Rb pathway is again inactivated via conditional expression of  $T_{121}$ , but this time under control of the MMTV promoter. The MMTV promoter also constrains expression of  $T_{121}$ , and thus Rb loss, to luminal epithelial cells. The same conditional models of p53 and BRCA1 loss are also utilized. Induction is achieved in adult mice by crossing with Wap-Cre transgenic mice, and subsequent pregnancy/lactation required to activate the Wap promoter (and therefore recombination). While tumor induction is no longer focal, it is penetrant. See Appendix B for more details.

This alternative strategy targets the same molecular pathways as the original strategy, including using  $T_{121}$  to inactivate pRb. However, it addresses the two problems above by using (i) the MMTV promoter to drive  $T_{121}$  expression, and (ii) the Wap-Cre strain to achieve efficient recombination during pregnancy and lactation. These models were developed by our collaborator, Dr. Karl Simin from the University of Massachusetts. His thorough characterization of these models (published in Kumar et al<sup>15</sup>, included in Appendix B) underscores the most important feature of the alternative GEM modeling strategy: it yields a series of highly penetrant mouse models of breast cancer and DCIS (Figure 8).



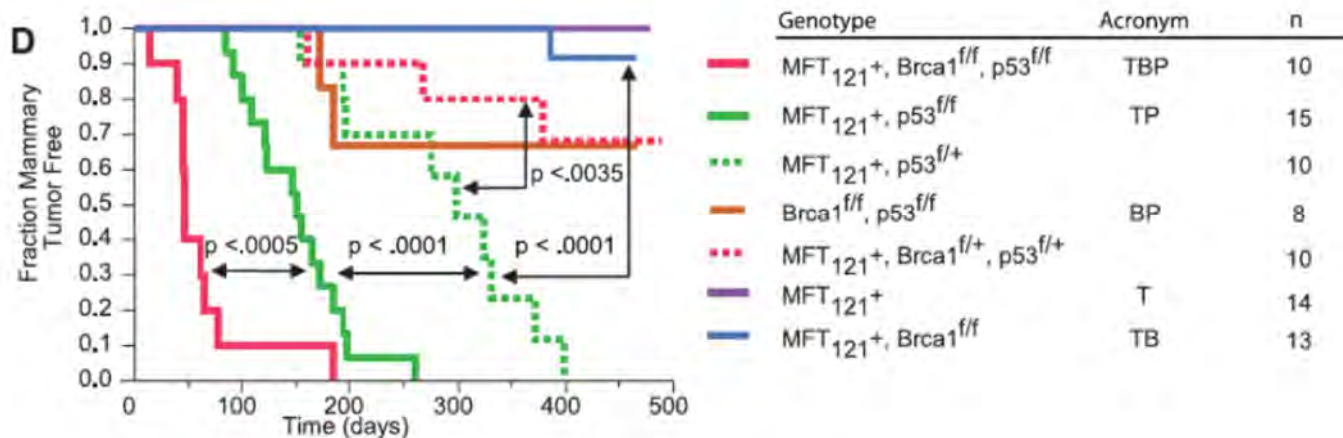


**Figure 8. Alternative GEM modeling strategy achieves penetrant tumor initiation with varying latency depending on genotype.** Figure from Kumar et al<sup>15</sup> characterizing tumor initiation and progression in different genotypes depending on which pathways (Rb, p53, BRCA1) are altered. For example, the solid red line represents inactivation or loss of all three pathways. This genotype is the most aggressive. In comparison, the solid green line represents loss of Rb and p53, which is less aggressive than the triple hit model. We propose to perform an image-based characterization of these different genotypes, to determine whether the MRI features of preinvasive malignancies correlate with molecular signatures. See Appendix B for more details.

Therefore, by using this alternative GEM modeling strategy we have identified an effective model system in which to test our hypotheses. We propose to perform an image-based characterization of these different genotypes, to determine whether the MRI features of preinvasive malignancies correlate with molecular signatures.

**Statement of Work (SOW).** The following Tasks from the SOW are applicable to the abbreviated reporting period and are presented below highlighted in grey. All tasks were completed, but not necessarily with the expected results.

**Task 1. Establish relevant inducible GEM model systems for preinvasive breast cancer by disruption of the pRb, BRCA1 and p53 pathways singly and in combination.** We seek to establish conditional GEMs reflecting different molecular drivers of tumorigenesis. To accomplish this, we have selected three pathways that are relevant to subsets of human breast cancer: pRb, p53 and BRCA1. We hypothesize that alteration of these pathways alone and in combination will generate a spectrum of molecular subtypes of preinvasive malignancies, including possibly those that are more indolent vs. aggressive (i.e., more slowly vs. rapidly progressing to invasive carcinoma). To achieve focal induction of tumorigenesis—which is desirable from an imaging perspective to facilitate accurate lesion detection and tracking—lentiviral mediated delivery of Cre recombinase into mammary epithelia will be performed.

**1a. Obtain regulatory approval (Months -3 to 0).** Upon notice of proposal approval we will commence the regulatory process.

Completed. Regulatory approval to generate sufficient numbers of mice (both [original GEM models](#) and [alternative GEM models](#)) and conduct the studies outlined in Task 1 was granted by the NCI-Frederick Animal Care and Use Committee, the NCI-Frederick Institutional Biosafety Committee and also through the DOD ACURO process.

**1b. Generate study mice (Months -3 to 2).** All of the mice needed to generate our study genotypes are already part of the Van Dyke stock colony. We will begin the breeding schema upon notice of proposal approval. A total of 5 genotypes will be studied, all on the FVB background inbred strain.

Completed. All of the [original GEM model](#) strains were generated in a homozygous state and breeder pairs established. In addition, breeder pairs for the [alternative GEM model](#) strains were obtained from our collaborator, Dr. Karl Simin, and re-derivation procedures commenced in order to house the mice as part of the Van Dyke colony and expand the cohort.

**1c. Optimize viral delivery of Cre recombinase via intraductal injection into Cre reporter mice (Months 1-3).** A total of **30 mice** (*RosaYFP*) will be used. Lentiviral-Cre recombinase at different titers and volumes will be injected into the nipple of inguinal glands. The dose that consistently delivers the highest recombination efficiency will be used for the remainder of the study.

Completed. As described in more detail below, we developed a new intraductal injection technique and evaluated recombination efficiency *in vitro* and *in vivo* for two different lenti-Cre constructs (pBob-CAG-iCre-SD and rrl-CMV-Cre-SD), packaged by two different institutions (SBI and the Salk Institute) at approximately  $10^9$  PFU/ml. Our *in vitro* results identified the most effective lenti-Cre construct as the pBOB-CAG-iCre-SD packaged by the Salk Institute. However, *in vivo* evaluation of this construct injected into the mammary glands of *RosaYFP* Cre reported mice demonstrated poor recombination efficiency, thereby necessitating a change in plan to the [alternative GEM modeling strategy](#).

**[New no-incision intraductal injection technique:](#)** Previously reported intraductal injection techniques involve a y-incision along the lower belly of the mouse, holding the cut skin taught, injecting into the #4 and #9 inguinal gland nipples, and then using wound clips to close the incision<sup>16</sup>. Such injection techniques do not permit experimental manipulation of the animal for approximately 10 days due to the necessity of waiting for the wound to heal. In addition, there is potential for harm to the animal during and after the y-incision intraductal injection procedure. To avoid these limitations, we developed a no-incision intraductal injection technique wherein the y-incision is avoided and injections are performed directly into the #4 and #9 inguinal gland nipples (Figure 9). We optimized this technique so that it was successful approximately 60% of the time when injected in 8-10 week old mice (matching previous reported performance using the y-incision method). A total volume of 10-20 $\mu$ l could be injected without damaging the ductal tree. This no-incision approach has the added advantage of being less harmful to the animals, and allowing experimental manipulation (e.g., MRI) to occur immediately after injection, rather than waiting 10 days for removal of wound clips.

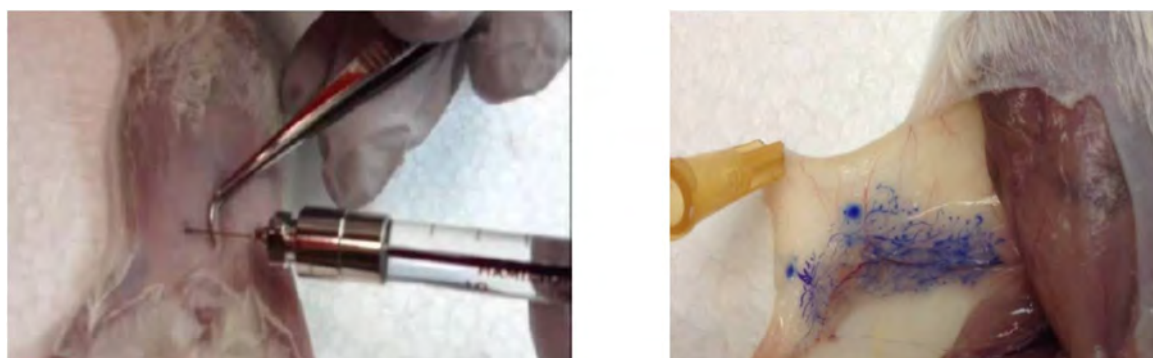


**Figure 9: No-incision intraductal injection technique.** Blue dye was injected into the #9 inguinal nipple of a 10 week old FVB mouse (left). Ex vivo examination demonstrates intact ductal tree (right).





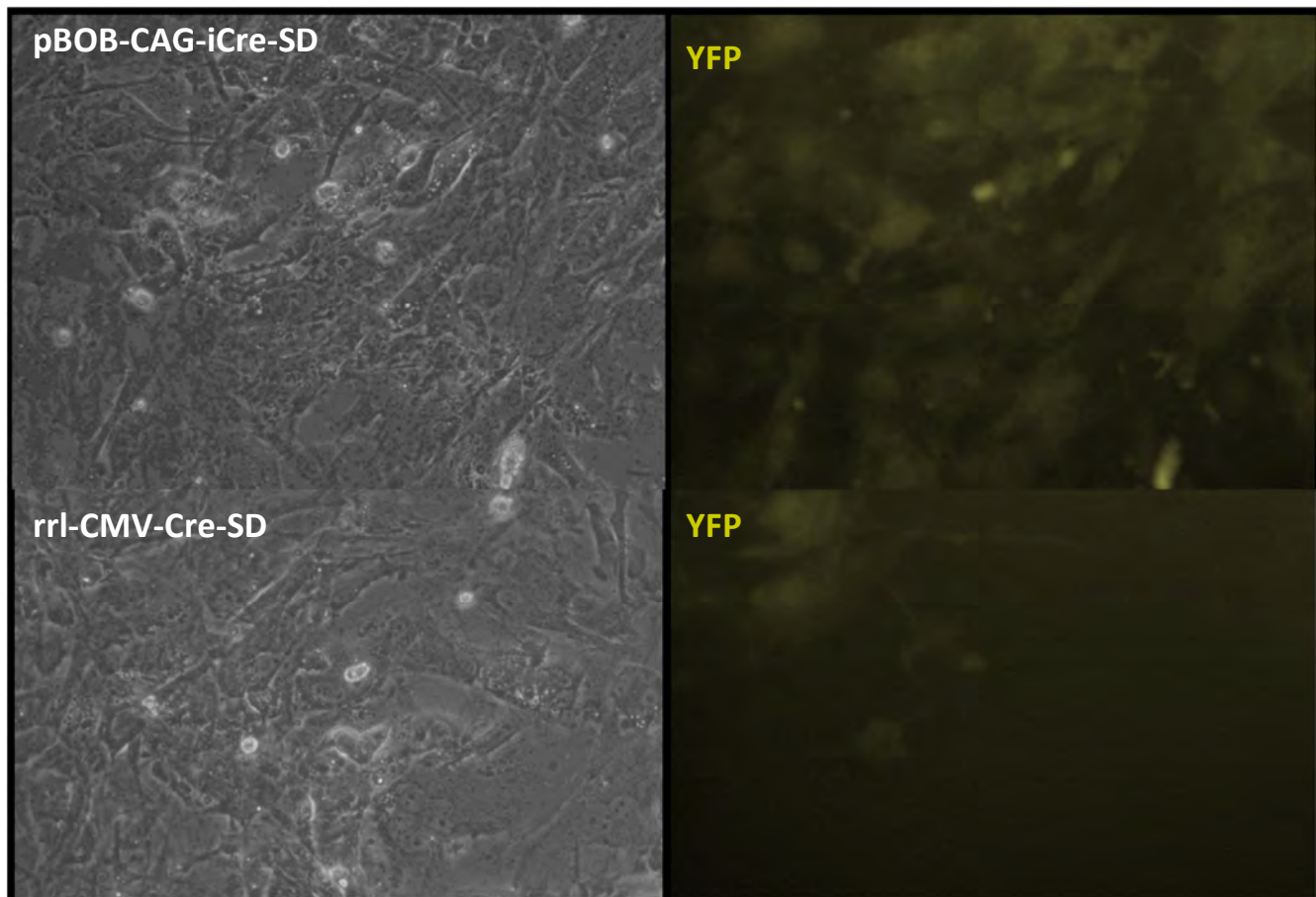


**Figure 11. Improved recombination efficiency using the pBOB-CAG-iCre-SD construct.** RosaYFP MEFS were cultured and infected with 200 MOI of each construct. MEFS were examined at 1 and 2 weeks post infection for YFP expression (i.e., evidence for recombination).

*In vivo evaluation of lenti-Cre recombination efficiency:* Inguinal mammary glands of n=14 8-10 week old RosaYFP Cre reporter mice were injected with 10 $\mu$ l of the pBOB-CAG-iCre-SD ( $\sim 10^7$  PFU) and were examined at 4 weeks and 2 months post injection for analysis of YFP expression i.e., evidence of recombination. YFP expression by IHC was not detected. Therefore, *in vivo* evaluation of the most promising lenti-Cre candidate demonstrated at most very poor recombination efficiency when injected into adult mammary glands. These results prompted us to revisit our original plan and design an alternative GEM modeling strategy which avoids the use of lenti-Cre for recombination.

**1d. Evaluate optimized dose in study mice (Months 3-6).** A total of **30 mice** will be used. Lentiviral-Cre will be delivered via intraductal injection and recombination will be monitored by PCR of genomic DNA and by IHC for T<sub>121</sub> expression.

Completed. Using the no-incision intraductal injection technique developed in Task 1c, we injected n=22 mice from the original GEM model with 10 $\mu$ l of the pBOB-CAG-iCre-SD ( $\sim 10^7$  PFU). Excised mammary glands were examined by IHC at 2 weeks, 4 weeks and 2 months post injection to evaluate for T<sub>121</sub> expression, and therefore Rb inactivation. T<sub>121</sub> protein expression was not visualized, further confirming the poor recombination efficiency achieved by lentiviral mediated Cre delivery in the adult mouse mammary gland.

**Task 2. Perform clinically relevant magnetic resonance imaging characterization of preinvasive neoplasias and correlate with genotype and molecular features.**

**2a. Obtain regulatory approval (Months -3 to 0).** Upon notice of proposal approval we will commence the regulatory process.

Completed. Regulatory approval to conduct the studies outlined in Task 2 was granted by the NCI-Frederick Small Animal Imaging Program, NCI-Frederick Animal Care and Use Committee, the NCI-Frederick Institutional Biosafety Committee and also through the DOD ACURO process.

**2b. Effect of virus injection on MRI of the normal mammary gland (Months 3-6).** A total of **10 mice** of the FVB inbred strain will be used. Right side inguinal glands will be injected with lentiviral Cre and compared with left side uninjected glands on MRI.

Completed. The right inguinal glands of n=10 8-10 week old FVB mice were injected with 10 $\mu$ l of the pBOB-CAG-iCre-SD ( $\sim 10^7$  PFU) using the no-incision intraductal injection technique. These mice were imaged 19 days later using a **noncontrast T<sub>1</sub> 3D MRI protocol** (T1 FFE, 3D, TR/TE 26/2.9ms, in plane resolution=0.2 mm, slice thickness=0.4 mm, field of view (FOV)=30 $\times$ 20 $\times$ 9 mm, number of excitations (NEX)=8, flip angle (FA)=25 $^\circ$ , no respiratory gating). There were no qualitative or quantitative (SNR) differences found in the MRI presentation of the right (injected) and left (uninjected) inguinal glands. Therefore, injection with lentiviral-Cre does not result in a long-term measurable difference in the MRI presentation of the normal mouse mammary gland.

**2c. Sensitivity/specificity study and DCEMRI (Months 7-24).** The same mice from Task 1e will be used. Mice will be imaged with rapid noncontrast T<sub>1</sub> 3D MRI and high temporal resolution dynamic contrast enhanced MRI (DCEMRI). The rapid noncontrast T<sub>1</sub> 3D images will be compared with pathologic evaluation to calculate the sensitivity/specificity of MRI. The DCEMRI data will be analyzed using several clinically relevant quantitative parameters.

Task 2c commences at Month 7 of the SOW, and therefore falls outside of the 6 month reporting period. Nonetheless, some progress was made in this subtask with regards to imaging technique development. As noted above, our original GEM modeling strategy did not yield effective mouse models of DCIS due to an insufficient initiating event. Without an effective mouse model, imaging technique development is not possible. Therefore, after obtaining DOD ACURO approval via a modification request (see Appendix A) we turned to the C3(1) SV40 Tag mouse model of breast cancer for imaging technique development; see the draft manuscript in Appendix C for more details. To summarize the study, we developed a high resolution, multi-modality strategy for imaging preinvasive mammary neoplasias in the C3(1) SV40 Tag GEM model. We performed high resolution MRI on a 3Tesla clinical scanner, using noncontrast T<sub>1</sub> and T<sub>2</sub> weighted acquisitions and dynamic contrast enhanced MRI. Preinvasive lesions were readily identified on noncontrast T<sub>1</sub> and T<sub>2</sub> weighted acquisitions. Subsequently, MRI-directed ultrasound was performed and an agar grid was used to correlate MRI with ultrasound and histology. We found that both MRI and ultrasound were able to detect preinvasive neoplasias with high sensitivity (over 90% in the posterior inguinal mammary glands). This study established an imaging strategy for monitoring mouse models of DCIS, with rapid imaging acquisitions in two different modalities. This work sets the stage for combining advanced imaging and mouse modeling techniques to gain relevant insights on image-based biomarkers of DCIS. We also performed a pilot serial imaging study in n=10 C3(1) Tag mice to demonstrate the feasibility of using noncontrast T1 3D MRI to follow lesion development over time (over two months, imaging the mice every few days). Our plan was to apply these imaging strategies to the alternative GEM models, so as to achieve our goal of investigating the capacity for quantitative *in vivo* MRI features to represent underlying molecular signatures of DCIS. Note that the MRI datasets acquired from the C3(1) Tag mice were compiled into a publically available database in the Mouse Mammary collection of the National Biomedical Imaging Archive (NBIA) to facilitate sharing of our results with the larger breast cancer research community.

## KEY RESEARCH ACCOMPLISHMENTS

The following key research accomplishments were achieved during the abbreviated 6 month reporting period:

- New no-incision intraductal injection technique was developed and optimized. With an over 60% success rate, this new approach matches the reported efficacy of the y-incision intraductal injection technique, while minimizing the duress to the mouse and expanding the opportunity for experimental manipulation to occur shortly after injection. Although the lentiviral mediated delivery of Cre recombinase proposed in the original GEM modeling strategy was found to be inefficient, the no-incision intraductal injection technique can be used for a wide range of purposes. It has been shared with several of our very interested collaborators.
- New MRI and multimodality imaging techniques for preinvasive mouse mammary cancer were developed and optimized (see Appendix C). This includes highly sensitivity (over 90%) and rapid (~5 minute acquisition) screening MRI techniques for detection preinvasive malignancies in a GEM model.

## REPORTABLE OUTCOMES

The following reportable outcomes were achieved during the abbreviated 6 month reporting period:

- New database of mouse mammary gland MR images, uploaded to the National Biomedical Imaging Archive (<https://wiki.nci.nih.gov/display/CIP/Mouse+Mammary>). The Mouse Mammary Collection consists of 25,998 MR images of mouse mammary glands. It has been placed on the web-accessible NBIA to facilitate sharing of our research findings with the larger community
- Manuscript draft in preparation, summarizing the efficacy of MRI for detection and characterization of preinvasive mammary cancers in mice (see Appendix C).
- New employment. The PI on this grant accepted a new permanent position with the breast imaging group at the U.S. Food and Drug Administration in February 2013. Obtaining this DOD Postdoctoral Award was an important qualification for the new position, as it underscored her interdisciplinary training and expertise in medical physics, breast cancer biology and animal modeling.

## CONCLUSION

Our main goal in this proposal was to investigate the capacity for quantitative *in vivo* MRI features to represent underlying molecular signatures of DCIS, using the preclinical GEM model framework to our hypotheses. We were particularly interested in three key molecular pathways—Rb, p53, BRAC1—and whether MRI signatures can identify these molecular subtypes of disease. Early on in our endeavors as we executed the Tasks outlined in the SOW, we discovered limitations in our original GEM modeling strategy suggesting that our proposed studies could not be effectively performed. We therefore designed an alternative GEM modeling strategy that successfully addressed these limitations. We also developed novel MRI techniques to detect, characterize and follow progression of the preinvasive malignancies in the mouse mammary gland at high spatial resolution, and high frequency (rapidly imaging every few days). Although a new employment opportunity resulted in the duration of this award being cut short, the progress made in the first six months of this award, including the pitfalls and solutions, was exciting and informative.

## REFERENCES

1. Liu X, Holstege H, van der Gulden H, et al: Somatic loss of BRCA1 and p53 in mice induces mammary tumors with features of human BRCA1-mutated basal-like breast cancer. *Proc Natl Acad Sci U S A* 104:12111-12116, 2007.
2. Saenz-Robles MT, Sullivan CS, Pipas JM: Transforming functions of Simian Virus 40. *Oncogene* 20:7899-7907, 2001.
3. Herschkowitz JI, Simin K, Weigman VJ, et al: Identification of conserved gene expression features between murine mammary carcinoma models and human breast tumors. *Genome Biol* 8:R76, 2007.
4. Simin K, Wu H, Lu L, et al: pRb inactivation in mammary cells reveals common mechanisms for tumor initiation and progression in divergent epithelia. *PLoS Biol* 2:E22, 2004.
5. Hill R, Song Y, Cardiff RD, Van Dyke T: Selective evolution of stromal mesenchyme with p53 loss in response to epithelial tumorigenesis. *Cell* 123:1001-1011, 2005.
6. Hill R, Song Y, Cardiff RD, Van Dyke T: Heterogeneous tumor evolution initiated by loss of pRb function in a preclinical prostate cancer model. *Cancer Res* 65:10243-10254, 2005.
7. Xiao A, Yin C, Yang C, Di Cristofano A, Pandolfi PP, Van Dyke T: Somatic induction of Pten loss in a preclinical astrocytoma model reveals major roles in disease progression and avenues for target discovery and validation. *Cancer Res* 65:5172-5180, 2005.
8. Xiao A, Wu H, Pandolfi PP, Louis DN, Van Dyke T: Astrocyte inactivation of the pRb pathway predisposes mice to malignant astrocytoma development that is accelerated by PTEN mutation. *Cancer Cell* 1:157-168, 2002.
9. Armitage P, Behrenbruch C, Brady M, Moore N: Extracting and visualizing physiological parameters using dynamic contrast-enhanced magnetic resonance imaging of the breast. *Med Image Anal* 9:315-329, 2005.
10. Bhooshan N, Giger ML, Jansen SA, Li H, Lan L, Newstead GM: Cancerous breast lesions on dynamic contrast-enhanced MR images: computerized characterization for image-based prognostic markers. *Radiology* 254:680-690, 2010.
11. Uematsu T, Kasami M, Yuen S: Triple-negative breast cancer: correlation between MR imaging and pathologic findings. *Radiology* 250:638-647, 2009.
12. The Cancer Genome Atlas. Comprehensive molecular portraits of human breast tumours. *Nature* 490:61-70, 2012.
13. Allred DC, Wu Y, Mao S, Nagtegaal ID, Lee S, Perou CM, Mohsin SK, O'Connell P, Tsimelzon A, Medina D. Ductal carcinoma in situ and the emergence of diversity during breast cancer evolution. *Clin Can Res* 14:370-8 2008.
14. Knudsen ES, Pajak TF, Qeenan M, McClendon AK, Armon BD, Schwartz GF, Witkiewicz AK. Retinoblastoma and phosphate and tensin homolog tumor suppressors: impact on ductal carcinoma in situ progression. *J Natl Cancer Inst.* 2012 Dec 5;104(23):1825-36.
15. Kumar P, Mukherjee M, Johnson JP, Patel M, Huey B, Albertson DG, Simin K. Cooperativity of Rb, Brca1, and p53 in malignant breast cancer evolution. *PLoS Genet.* 2012;8(11).
16. Behbod F, Kittrell FS, LaMarca H, Edwards D, Kerbawy S, Heestand JC, Young E, Mukhopadhyay P, Yeh HW, Allred DC, Hu M, Polyak K, Rosen JM, Medina D. An intraductal human-in-mouse transplantation model mimics the subtypes of ductal carcinoma in situ. *Breast Cancer Res.* 2009;11(5).

## APPENDICES

The following appendices provide relevant supplementary information to what has been presented in this report.

- Appendix A: Approved modification request submitted to the DOD proposing our alternative GEM modeling strategy
- Appendix B: Published article from the group of our collaborator, Dr. Karl Simin, providing additional

information on our alternative GEM modeling strategy

- Appendix C: Manuscript draft on imaging technique development in C3(1) SV40 Tag mice



**Modification request for BC112281:** *Investigating ductal carcinoma in situ using noninvasive imaging of genetically engineered mouse models.*

### **Background/Justification**

The key scientific element in Specific Aim #1 is to establish mouse models of preinvasive breast cancer by disrupting the *Rb*, *BRCA1* and *p53* pathways singly and in combination. We contend that these genetic events will produce diverse preinvasive mammary carcinomas that can be studied with noninvasive imaging (in Specific Aim #2). Based on our extensive experience in many tissue types, inactivation of the *Rb* tumor suppressor pathway is likely the critical initiating event for tumorigenesis; additional loss of *BRCA1* and *p53* are likely progressing events. We proposed to utilize two novel tools for implementing these genetic events in the mouse:

- ***Using T121 protein to inactivate the Rb family for tumor initiation.*** Inactivation of the Rb tumor suppressor family (which includes Rb, p107, p130) is a critical step for cancer initiation. We use a novel protein T121 to functionally inactivate all three family members, which is a much more efficient route to Rb inactivation than genetic deletion. We proposed to use a keratin 18 (K18) promoter to target conditional T121 expression to luminal epithelial cells (*K18-eGT<sub>121</sub>tg/+* mice).
- ***Using viral-Cre mediated tumor induction.*** The proposed mouse models are conditional, meaning that the genetic mutations occur only after exposure to Cre recombinase. In this way, the timing of malignant transformation can be experimentally controlled. We proposed to deliver Cre recombinase using lentiviral vectors. This has the advantage of inducing tumorigenesis focally, which would greatly improve our capacity to image single lesions over time.

However, recent evidence obtained in the past several months suggests that our initially proposed strategy may not efficiently induce tumor initiation:

- ***Limitation 1: Using the K18 promoter to express T121 is inefficient for tumor initiation.*** *K18-eGT<sub>121</sub>tg/+* mice only weakly express T121 in mammary epithelial cells, and thus may not inactivate the *Rb* family sufficiently for tumor initiation
- ***Limitation 2: Using viral-Cre is inefficient for tumor induction.*** Lentiviral delivery of Cre recombinase inefficiently induces recombination and thus tumorigenesis. Indeed, this was an anticipated pitfall we acknowledged in our proposal: “*Technically, the most significant potential pitfall is that the lentiviral-Cre may not be sufficiently effective to induce tumorigenesis... Given our desire for focal induction, we will first evaluate other viral vectors for delivery and subsequently try a mammary specific Cre line, such as WAP-Cre transgenic mice.*”

These recent technical developments may significantly impact the efficacy of our initially proposed strategy, as it will delay or perhaps even preclude a tumor phenotype from developing.

### **Modification request**

We thus propose the following modifications that will ensure a much higher likelihood of success in testing our scientific hypotheses:

- ***Modification 1: Use MMTV-eGT<sub>121</sub>tg/+ mice, demonstrated to efficiently express T121 and yield mammary tumor initiation.*** These mice, developed by our collaborator Dr. Karl Simin, use the MMTV promoter to target conditional T121 expression to luminal mammary epithelial cells. We plan to obtain from Dr. Simin either live mice or frozen materials for rederivation. Dr.

Simin has successfully used these mice to initiate mammary tumorigenesis, including in the context of additional *BRCA1* and *p53* loss (results are now *in press*, PLoS Genetics). Therefore, we are highly confident that *MMTV-eGT<sub>121</sub>tg/+* mice will efficiently yield tumor initiation, thereby mitigating Limitation #1 noted above.

- ***Modification 2: Use other Cre delivery strategies demonstrated to be effective in the mammary gland.*** As stated in our proposal, in addition to evaluating other lenti-Cre constructs, we will utilize mammary specific Cre lines for genetic recombination, specifically WAP-Cre and K14Cre, which are widely utilized in mouse models of breast cancer (Liu et al. PNAS 2007, Li et al. Cancer Cell 2007). In doing so, we will mitigate Limitation #2 noted above.
- ***Modification 3: Concurrent imaging technique development with C3(1)SV40Tag mice.*** Specific Aim #2 of our proposal involves a significant component of imaging technique development prior to the image-based characterization of our T121-based mouse models. The heretofore described limitations and modifications imply that it may be some time before we can use the T121-based models for this purpose. To facilitate timely completion of our aims according to the SOW, we thus propose to use the C3(1)SV40Tag transgenic mouse model of breast cancer (Green et al, Oncogene 2000) for imaging technique development. In this way, once we have implemented Modifications 1 and 2 we will be ready to proceed with the image-based characterization of our T121-based mouse models.

We are not revising the scientific purpose, methodology or evaluation outlined in the original proposal. Importantly, the targeted genetic events are not changed—*Rb* pathway inactivation, *BRCA1* loss and *p53* loss. Rather, these minor modifications alter some of the technical methods used to achieve the same scientific ends. These technical modifications will put us in a much stronger position to test our scientific hypotheses.

# Cooperativity of *Rb*, *Brca1*, and *p53* in Malignant Breast Cancer Evolution

Prashant Kumar<sup>1</sup>, Malini Mukherjee<sup>2</sup>, Jacob P. S. Johnson<sup>1</sup>, Milan Patel<sup>1</sup>, Bing Huey<sup>3</sup>, Donna G. Albertson<sup>3</sup>, Karl Simin<sup>1\*</sup>

<sup>1</sup> Department of Cancer Biology, University of Massachusetts Medical School, Worcester, Massachusetts, United States of America, <sup>2</sup> Department of Pediatric Hematology/Oncology, Texas Children's Cancer Center, Baylor College of Medicine, Houston, Texas, United States of America, <sup>3</sup> Helen Diller Family Comprehensive Cancer Center, University of California San Francisco, San Francisco, California, United States of America

## Abstract

Breast cancers that are “triple-negative” for the clinical markers ESR1, PGR, and HER2 typically belong to the Basal-like molecular subtype. Defective *Rb*, *p53*, and *Brca1* pathways are each associated with triple-negative and Basal-like subtypes. Our mouse genetic studies demonstrate that the combined inactivation of *Rb* and *p53* pathways is sufficient to suppress the physiological cell death of mammary involution. Furthermore, concomitant inactivation of all three pathways in mammary epithelium has an additive effect on tumor latency and predisposes highly penetrant, metastatic adenocarcinomas. The tumors are poorly differentiated and have histologic features that are common among human *Brca1*-mutated tumors, including heterogeneous morphology, metaplasia, and necrosis. Gene expression analyses demonstrate that the tumors share attributes of both Basal-like and Claudin-low signatures, two molecular subtypes encompassed by the broader, triple-negative class defined by clinical markers.

**Citation:** Kumar P, Mukherjee M, Johnson JPS, Patel M, Huey B, et al. (2012) Cooperativity of *Rb*, *Brca1*, and *p53* in Malignant Breast Cancer Evolution. PLoS Genet 8(11): e1003027. doi:10.1371/journal.pgen.1003027

**Editor:** Sharon E. Plon, Baylor College of Medicine, United States of America

**Received:** February 10, 2012; **Accepted:** August 23, 2012; **Published:** November 15, 2012

**Copyright:** © 2012 Kumar et al. This is an open-access article distributed under the terms of the Creative Commons Attribution License, which permits unrestricted use, distribution, and reproduction in any medium, provided the original author and source are credited.

**Funding:** This work was supported by ACS IRG-93-033-15, the Simeon J. Fortin Charitable Foundation, charitable contributions by N. Ekross and Dr. S. Gupta to KS, and NIH CA84118 to DGA. The funders had no role in study design, data collection and analysis, decision to publish, or preparation of the manuscript.

**Competing Interests:** The authors have declared that no competing interests exist.

\* E-mail: karl.simin@umassmed.edu

## Introduction

The dire need for more effective treatments for aggressive breast cancers has motivated intensive investigations into their cellular and molecular etiology. Breast cancers classified as “triple-negative” by clinical diagnostic markers (ESR1, PGR, and HER2 negative) are heterogeneous in their clinical behavior, morphology, and molecular biology. Triple-negative breast cancers (TNBC) typically express the Basal-like molecular signature, thus TNBC and Basal cancer classifications are frequently used interchangeably. However, they are not completely synonymous [1,2]. TNBCs also include the Claudin-low molecular subtype [3], which is characterized by greatly reduced expression of intercellular junction components and by activation of molecular pathways associated with epithelial-to-mesenchymal transition (EMT), cancer stem cells, and the immune response [4].

Histologically, most triple-negative breast cancers are invasive ductal carcinomas, but TNBCs also include the metaplastic, medullary, and adenocystic histologic special types, distinctive morphologies that are prevalent among Claudin-low tumors [4]. TNBCs are insensitive to endocrine therapy and HER2 antagonists, but they are sensitive to chemotherapy. Nevertheless, long-term patient outcomes are poor due to high rates of relapse and acquired chemoresistance [5,6]. Mouse models that mimic the complexity of TNBC will be invaluable tools for defining the diverse cellular biology and behavior of these tumors and for rigorously triaging new drug candidates.

Basal-like breast cancers often simultaneously inactivate three tumor suppressors that are infamous for their roles in familial

cancers: *Rb* (*RBI*) [7], *p53* (*TP53*) [8], and *BRCA1* [9]. *p53* is mutated in 20–30% of human breast cancers and defective pathway intermediates also increase breast cancer risk [10]. Moreover, nearly all Basal-like cancers with *BRCA1* mutation have concomitant *p53* mutation [11]. Germline *BRCA1* mutation predisposes early-onset breast cancers that are often triple-negative and that correlate with Basal-like tumors in microarray analyses [9]. *BRCA1* mutation accounts for nearly half of familial breast cancers (OMIM 604370), but *BRCA1* is also down-regulated in sporadic breast tumors without germline mutation [12]. The overall effect of *BRCA1* loss is likely pleiotropic. The best studied function of *BRCA1* is in orchestrating DNA double-strand break repair through homologous recombination or non-homologous end-joining. The importance of defective DNA repair in breast cancer is underscored by the observation that all known genes associated with inherited forms of the disease safeguard genomic integrity [13]. *BRCA1* also functions as a transcription factor [14] that appears to be required for the differentiation of stem/progenitor cells into mature luminal cells [15]. This finding is consistent with the recent characterization of *BRCA1*-associated tumors as aberrant luminal progenitor cells [16].

The pair-wise cooperativity of *Brca1* and *p53* in mammary tumorigenesis has been studied in mouse models [17]. We and others have investigated the impact of combined *Rb* and *p53* inactivation on mammary tumorigenesis *in vivo* [18–20]. We showed that following *Rb* perturbation *in vivo*, tumor progression is limited largely by *p53*-dependent apoptosis, and that loss of the second *p53* allele in *MFT<sub>121</sub>+/p53<sup>+/+</sup>* tumors is likely a prerequisite

## Author Summary

These studies establish a unique animal model of aggressive forms of breast cancer for which there are no effective, targeted treatments. *Rb*, *p53*, and *Brca1* are associated with inherited forms of cancer, but defects in these pathways are also found together in a subset of breast cancer patients without a family history of the disease. Simultaneous inactivation of all three pathways causes more aggressive disease than do pair-wise combinations, indicating that the pathways play non-overlapping roles in tumor prevention.

for mammary tumor progression [19], since the vast majority of tumors lose the wild type *p53* allele during tumorigenesis. In the context of a brain carcinoma model initiated by  $T_{121}$ , apoptosis appears to be the critical function of the normal *p53* allele that is the target of selective pressure [21].

Our motivation to combine *Rb* inactivation with *Brca1* and *p53* mutation derives, in part, from the observation that the *Rb* gene is among the most frequently deleted loci in *Brca1/p53*-mutated mouse tumors [22], indicating that *Rb* is a critical barrier to tumor progression. *Rb* pathway inactivation is strongly associated with human triple negative breast cancers. A cardinal feature of basal-like breast cancers is the abundant expression of the “proliferation cluster” genes [7], which include many E2F-regulated genes that are de-repressed following *Rb* inactivation. In human breast cancers, reduced pRb activity correlates with higher tumor grade [23], but also predicts improved chemotherapy responsiveness [24]. The *Rb* gene itself is mutated in breast cancer [25], and recent genomic studies have indicated an overrepresentation of mutations within pRb-binding sites of human gene regulatory domains [26].

In this study we show that mammary tumors caused by inactivation of the *pRb* family (pRb<sub>f</sub>) of proteins (pRb, p107, p130), together with *Brca1* and *p53* inactivation, mimic several aspects of the most aggressive forms of breast cancer, including rapid tumor progression, poor differentiation, distant metastasis, necrosis, metaplasia, and genomic instability. Our findings illustrate the compounding effect of acquiring multiple tumor suppressor mutations during tumor evolution and underscore the distinct requirements of each of these canonical tumor suppressor proteins.

## Results

### Conditional $T_{121}$ expression in mammary epithelium

We constructed the *MFT<sub>121</sub>* (MMTV-Floxed-eGFP- $T_{121}$ ) transgene to conditionally inactivate the pRb family (pRb<sub>f</sub>) of pocket proteins in mammary epithelium (Figure 1A). The  $T_{121}$  protein is an amino-terminal fragment of the SV40 large T antigen that perturbs pRb<sub>f</sub> activity and predisposes tumorigenesis in a range of tissues [27]. While *Rb* inactivation alone is sufficient to induce mammary tumors [20], the shorter latency of *TgWap-T<sub>121</sub>* tumors indicates there is functional redundancy or compensation by the related pocket proteins p107 or p130 [19]. In the *MFT<sub>121</sub>* model, the MMTV-LTR promotes mammary-specific transgene expression (Figure 1B). The approach of inactivating pRb<sub>f</sub>, *Brca1*, and *p53* specifically in mammary epithelial cells via the *Wap-Cre* transgene [28] enabled us to avoid the appearance of lymphomas [20] or sarcomas [29]. Wap-Cre excised the LoxP-eGFP-stop-LoxP reporter cassette and initiated  $T_{121}$  expression in ductal and alveolar luminal epithelial cells (Figure 1C). Virgin glands of *MFT<sub>121</sub>*; WAP-Cre mice appeared normal. Lactating glands (WAP-Cre-induced) showed reduced alveolar density, similar to the gland atrophy phenotype in the *TgWap-T<sub>121</sub>* model, which was associated

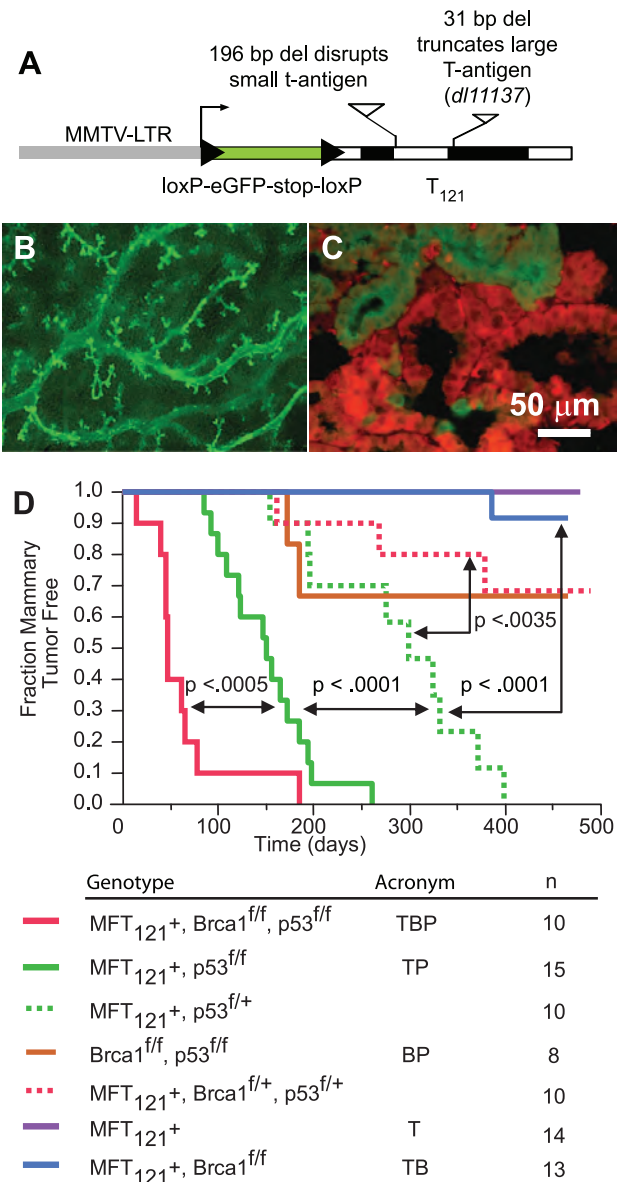


**Figure 1. The *MFT<sub>121</sub>* transgene construct.** (A) The *MFT<sub>121</sub>* transgene construct. The “floxed” eGFP-stop cassette was expressed throughout virgin mammary epithelium (B, original magnification 50×). Following Cre-induced excision,  $T_{121}$  was expressed (red) in the majority of luminal epithelial cells (C). eGFP immunolabeling (green) revealed non-recombined cells (original mag. 400×). Kaplan-Meier analysis of tumor onset (D). *p53* was haploinsufficient (dashed green) for tumor suppression ( $p < 0.0001$ , log-rank test). Homozygous *p53* mutation (solid green) shortened tumor latency. *Brca1* loss (solid red) further accelerated tumor onset ( $p < 0.0005$ ). Median tumor latency of TBP mice was approximately seven weeks. Parturition Day 1 = Time 0. All mice harbored the Wap-Cre transgene (not shown). Significance levels for critical comparisons are indicated. doi:10.1371/journal.pgen.1003027.g001

with apoptosis caused by  $T_{121}$ -induced proliferation [19] and lactation defects observed in WAP-Cre; *Rb<sup>fl/fl</sup>*; *p107<sup>-/-</sup>* mice [20].

### Concomitant *pRb*, *p53*, and *Brca1* inactivation significantly accelerates tumor onset

Multiparous *TgMFT<sub>121</sub>*; *TgWap-Cre* mice remained tumor-free for more than a year after Cre-induction, but mice that were either

heterozygous or homozygous for a conditional *p53* allele [30] (*TgMFT<sub>121</sub>; TgWAP-Cre; p53<sup>f/+</sup>* or *TgMFT<sub>121</sub>; TgWAP-Cre; p53<sup>f/f</sup>*) developed mammary tumors with 100% penetrance and clear evidence of *p53* haploinsufficiency (Figure 1D,  $p < 0.0001$ , log-rank test). Heterozygous *p53* mice developed tumors with a median latency of 299 days, while *p53* homozygous mice had a median tumor latency of 150 days. These results are consistent with previous findings that *p53* activity is rate limiting for mammary tumor progression initiated by *Rb* inactivation [18–20]. In contrast to the high penetrance we previously found in our *TgWAP-T<sub>121</sub>* breast tumor model [19], the present studies indicate that the *TgMFT<sub>121</sub>* transgene only partially inhibits pRb<sub>f</sub> pathways, possibly owing to the reduction in the transgene gene copy number following Cre excision. Similar dosage effects were observed in a conditional *T<sub>121</sub>* transgenic model of astrocytoma [31].

*Brca1* mutation dramatically accelerated tumor onset in mice with Rb<sub>f</sub>/p53 inactivation (Figure 1D,  $p < 0.0005$ ). Only a single mouse ( $n = 13$ ), doubly defective for *Rb<sub>f</sub>* and *Brca1* activity (*TgMFT<sub>121</sub>; TgWAP-Cre; Brca1<sup>f/f</sup>*), developed mammary tumors at 386 days following Cre induction by multiple pregnancies. In contrast, 100% ( $n = 10$ ) of *TgMFT<sub>121</sub>; Brca1<sup>f/f</sup> p53<sup>f/f</sup>; TgWAP-Cre* mice (hereafter, TBP) developed mammary tumors with a median latency of only 47 days. Thus, a single pregnancy was sufficient for 100% TBP tumor penetrance. Once palpable, TBP tumors grew rapidly to 1500 cc within several days (data not shown). Therefore, inactivation of the three canonical tumor suppressors showed additive effects on tumor latency, since TBP mammary tumors developed significantly faster than did pair-wise combinations.

### Enhanced survival and increased proliferation rates cause rapid tumor progression in *pRb/p53/Brca1*-perturbed epithelium

To investigate the early effects of tumor suppressor inactivation, we examined mammary gland biopsies ( $n = 5$  mice) from time points (0, 2, 6 weeks) following forced weaning at Day 1 parturition. At the earliest time point, *T<sub>121</sub>* expression alone was sufficient to cause benign, hyperproliferative lesions (Figure 2A, 2B). *T<sub>121</sub>*-expressing cells showed a higher Ki67 index than did cells without *T<sub>121</sub>*, as expected ( $p < 0.0063$ , Figure 3P). Combinations with *Brca1* and *p53* mutation caused higher grade, premalignant lesions (Figure 2C–2F). Tall columnar epithelia of darkly staining cells and papillary tufting (Figure 2C) were characteristic of the disrupted epithelial morphology. Pleomorphic, faintly staining nuclei with prominent nucleoli were common among *T<sub>121</sub>* expressing cells (Figure 3F).

The combined inactivation of pRb<sub>f</sub> and *p53* also dramatically suppressed the physiologic cell death of mammary involution (Figure 3I, 3N), although pRb<sub>f</sub> perturbation alone had little effect (Figure 3B, 3G, 3L). It was shown that *p53* mutation alone delayed involution by several days [32]. Here, we observed that the combined inactivation of pRb<sub>f</sub> and *p53* blocked involution through six weeks (Figure 3I, 3N). Biopsies from mice harboring *Brca1* mutation (Figure 3C, 3J) showed extensive cellular debris from dead or dying cells within their lumen. The dual loss of pRb<sub>f</sub> and *Brca1* activities (*TgMFT<sub>121</sub>; TgWAP-Cre; Brca1<sup>f/f</sup>*) triggered elevated cell death that was *p53*-dependent ( $p < 0.0001$ , Figure 3Q). The combined loss of pRb<sub>f</sub>, *Brca1*, and *p53* activities accelerated tumor progression, indicated by frank tumors that appeared by six weeks (Figure 3O). However, when measured at the earliest time point, neither an increased Ki67 proliferation index (Figure 3P) nor a decreased cell death index (Figure 3Q) presaged faster onset of TBP tumors compared to *Rb<sub>f</sub>/p53* tumors. Thus, full transformation occurred in only a minority cell

population, which likely reflects the requirement for additional collaborating oncogenic events.

### Histopathologic features of tumors with conditional inactivation of *pRb<sub>f</sub>*, *p53*, and *Brca1*

*T<sub>121</sub>/p53* (TP) and TBP mice developed high grade mammary adenocarcinomas with heterogeneous phenotypes indicative of highly perturbed differentiation, summarized in Table 1. Tumors of both genotypes showed mixed solid and glandular morphologies. More TBP mice than TP mice (13/14 vs. 8/16 cases,  $p = 0.0169$ , two-tailed Fisher's exact) developed solid tumors that were largely devoid of glandular architecture (Figure 4A). All solid tumors showed a mixture of pushing and infiltrative borders, and nearly half of the tumors were vascularized (Figure 4A). All carcinomas expressed varying levels of luminal epithelial markers, including Keratin-8 (Figure 4E, 4G, 4K) and E-Cadherin (Figure 4I, 4L). These markers were abundant in well-differentiated tumor regions but were greatly diminished or absent in poorly differentiated areas (Figure 4E, 4I, 4K, 4L). Nests of carcinoma cells variably expressed basal/myoepithelial lineage markers (Keratins-5, -14, Figure 4E, 4K).

Both TP and TBP mice (4/16 vs. 1/14 cases,  $p = 0.3359$ ) developed carcinosarcomas (Figure 4C), also known as “EMT” (Epithelial to Mesenchymal Transition) tumors [33]. These tumors are comprised of faintly-staining, fusiform, spindle cells and are characteristic of *p53* mutant mice. The histology of hematoxylin and eosin stained carcinosarcomas is relatively homogeneous and is visibly distinct from carcinomas with spindle metaplasia that showed biphasic carcinomatous and spindle morphologies (Figure 4B, 4G). Among both carcinosarcomas and metaplastic tumors, we observed dual expression of mesenchymal (Vimentin) and epithelial (Keratin-8) markers (Figure 4G), which are mutually exclusive lineage markers in the normal gland. Dual expression is also a feature of human Claudin-low [4] and mouse EMT tumors [33]. Poorly differentiated spindle cells along invasive tumor fronts showed either dual expression (Figure 4G) or greatly diminished epithelial marker expression (Figure 4J–4L).

In both TP and TBP tumors, we observed squamous metaplasia that was characterized by keratin nests (Figure 4M) and high expression of *Keratin 6* (Figure 4N), a marker of progenitor cells that is expanded in *Wnt-1*-induced mammary tumors. Four of fourteen cases (29%) of TBP tumors, but zero cases of TP tumors ( $p = 0.0365$ ), included whorls of spindle cells that resembled myoepithelial cells (not shown). Finally, central necrosis, a hallmark feature of human *BRCA1*-mutated tumors, was present in twelve of fourteen TBP cases, a greater proportion than the eight of sixteen *T<sub>121</sub>/p53* cases ( $p = 0.0577$ ), indicating that the selective pressure of cell death persists even in the absence of *p53* activity.

Distant metastases were observed in the lungs of both TP (4 of 14 cases) and TBP (3 of 6 cases) mice (Figure 4P), which is noteworthy because relatively few transgenic mammary tumor models metastasize. Among mouse models that do metastasize, most are derivatives of the PyMT model, which more closely resembles human Luminal subtype tumors than Basal-like tumors [3]. Metastases were not evident in the sternum, liver, or spleen of these mice. A primary cell line established from a TBP tumor formed secondary tumors following serial transplantation into syngeneic (FVB) mammary fat pads (Patel, unpublished), confirming the malignant capacity of TBP tumors.

In summary, TBP tumors displayed heterogeneous histology, including high grade, central necrosis, metaplasia, pushing borders, and metastasis, features that are characteristic of human *BRCA1*-mutated and Claudin-low breast tumors.



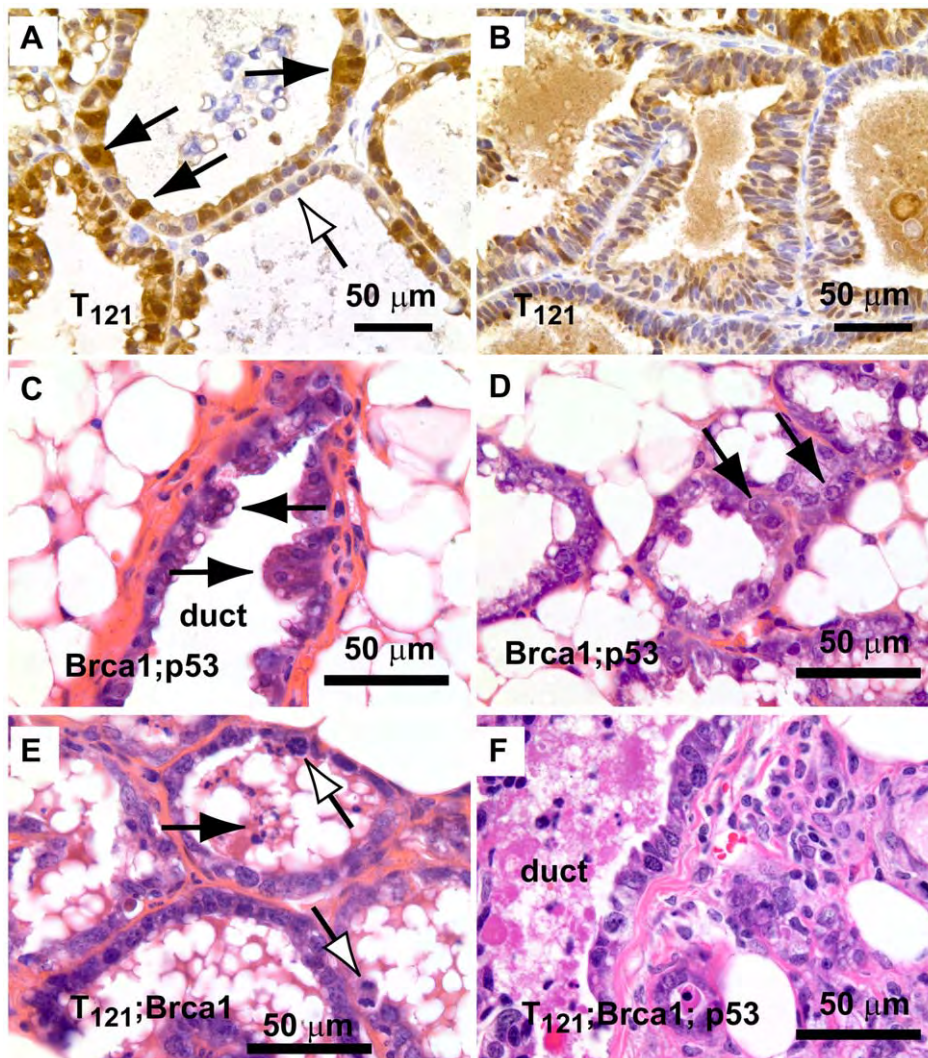


**Figure 2. Early lesions in lactating mammary glands.** (A) Nuclear and cytoplasmic  $T_{121}$  expression (brown) is associated with enlarged, pleiomorphic nuclei (filled arrows) compared to low-expressing cells (open arrow). (B) Benign, multi-layered, mammary intra-epithelial neoplasia (MIN) within the same gland as A. (C) Dual inactivation of *Brca1* and *p53* disrupted epithelial architecture in primary ducts (C) and lactating alveoli (D), shown by papillary tufting (C, arrows) and high grade nuclei and prominent nucleoli (D, arrows). High grade nuclei and mitotic figures (E, open arrows) and dead cell debris (arrow) in  $MFT_{121}; Brca1$  gland. Severely pleomorphic and high grade nuclei are visible throughout  $MFT_{121}; Brca1; p53$  gland (F).

doi:10.1371/journal.pgen.1003027.g002

### Global gene expression analysis

The majority of the  $TgMFT_{121}$  mouse tumors (76%) co-segregated with human Basal-like breast cancers by hierarchical clustering of the top ~1000 most variable genes in a combined data set of mouse ( $n = 135$ ) and human ( $n = 337$ ) tumor expression profiles (Figure 5, Figure S1, File S2). Using a similar approach that we reported previously [3], we assayed global transcript levels by microarray using tumors derived from TBP ( $n = 8$ ) and TP mice ( $n = 9$ ), and we compared them directly to tumors and normal tissue from other mouse models [3] and patient samples [4]. Two TP tumors clustered with human tumors that showed a mixture of the PAM50 molecular subtypes that were assigned by Prat and colleagues (2010). The two remaining TP tumors clustered with Claudin-low subtype human tumors.

The effect of *Brca1* mutation on TP tumors was more evident when we focused our analysis on the mouse specimens alone (Figure 6, File S3). 56% of the TP tumors (5 of 9) clustered with

mouse tumors that we previously showed resemble human Luminal tumors [3]. *Brca1* mutation shifted the tumor phenotype ( $p = 0.0529$ , Fisher's exact). All eight TBP tumors segregated with mouse tumors, including other *Brca1*-mutant models that more closely resemble human Basal-like TNBC (Figure 6A). TBP tumors and the other Basal-like mouse tumors expressed low levels of luminal markers and high levels of both Proliferation and Basal cluster transcripts, including *Keratins-14*, *-6b*, *-17* (Figure 6C). In contrast, the TP tumors that clustered with Luminal-B-like tumors (Figure 5A, blue box) showed higher expression of luminal marker genes that correlate with the estrogen pathway target *Xbp1* (Figure 5A). Interestingly, TBP tumors were distinct from most other Basal-like mouse tumors in their elevated expression of a subset of Claudin-low signature genes [3,4], including *Snail1*, *Tgfb1*, *Dtr*, and *Timpt1* (Figure 6C).

Four TP tumors (44%) did not segregate with Luminal-like tumors. This finding is consistent with previous reports by us and



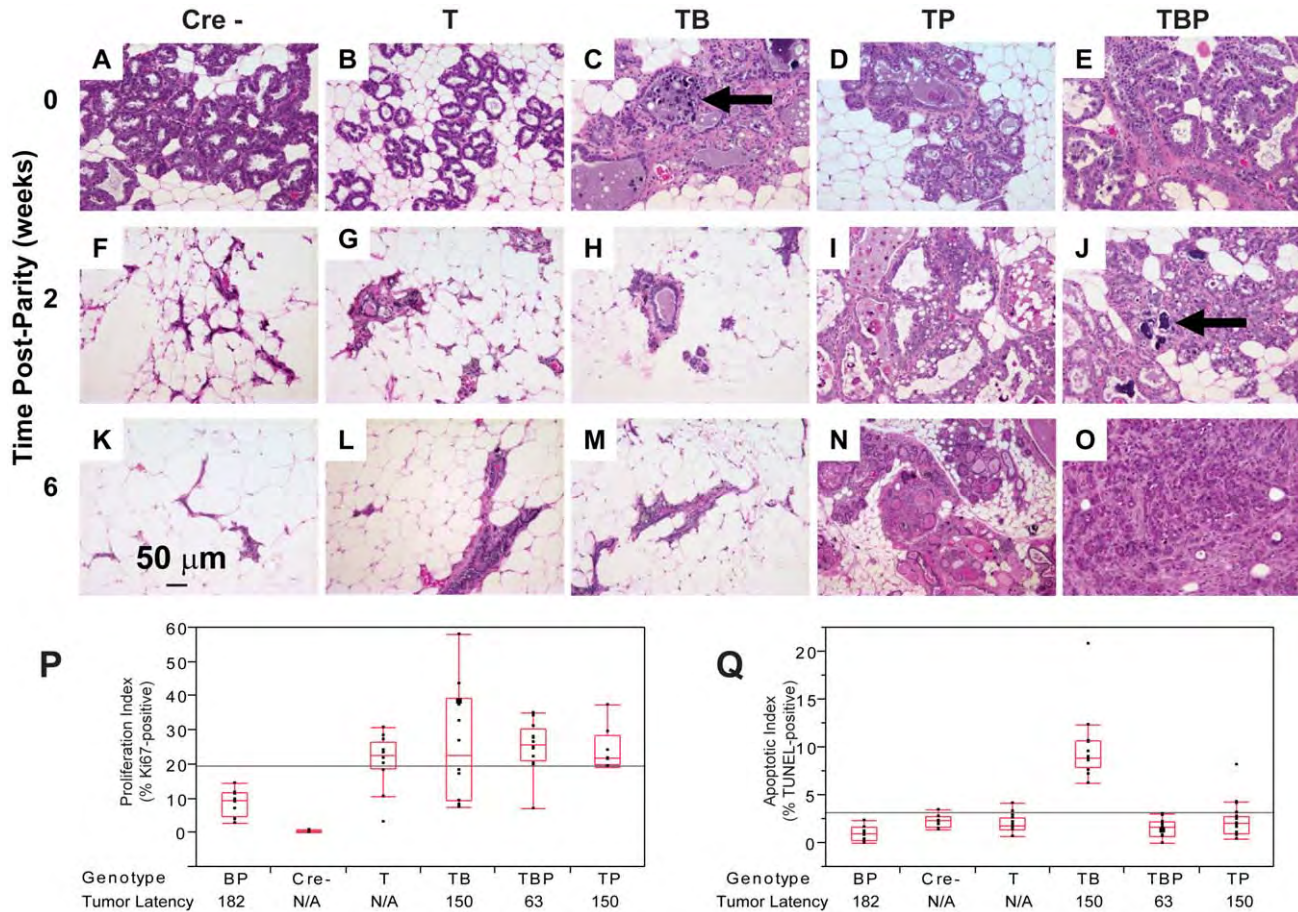


**Figure 3. Combined inactivation of *pRb* and *p53* causes a durable block in involution.** Lactating mammary epithelium of Cre-negative control mice (A, F, K) and *T<sub>121</sub>*-expressing mice (B, G, L) involute normally (A–E: 0 wks, F–J: 2 wks, K–O: 6 wks). *T<sub>121</sub>*-expressing mice have reduced alveolar density. Cell death and debris were abundant in TB glands (arrows panels C, J). TP glands failed to involute (N) and persisted as highly cystic glands. Frank tumors were present by 6 wks in TBP mice. An invasive adenocarcinoma fills the field of panel O. Measured at 0 wks, *T<sub>121</sub>* increased the Ki67 index but without added effect by *Brca1* and/or *p53* loss (P). Combined inactivation of *pRb* and *Brca1* increased TUNEL-positive cells, which was suppressed by *p53* loss (Q,  $p < 0.0001$ ). For each genotype  $n = 5$  mice. Original magnification of each panel was 200 $\times$ . T = *T<sub>121</sub>*, B = *Brca1*, P = *p53*. doi:10.1371/journal.pgen.1003027.g003

**Table 1. Characteristics of TP and TBP tumors.**

Histologic Feature	<i>TgMFT<sub>121</sub>, Brca1<sup>f/f</sup>, p53<sup>f/f</sup></i>	<i>TgMFT<sub>121</sub>, p53<sup>f/f</sup></i>	<i>TgMFT<sub>121</sub>, p53<sup>f/f</sup></i>
	n = 14 (%)	n = 11	n = 16
Solid*	13 (93)	6 (55)	8 (50)
Glandular	4 (29)	2 (18)	6 (38)
Spindloid metaplasia	9 (64)	4 (36)	5 (31)
Carcinosarcoma	1 (7)	3 (27)	4 (25)
Squamous Metaplasia	2 (14)	2 (18)	4 (25)
Myoepithelioma*	4 (29)	0 (0)	0 (0)
Cribriform	0 (0)	1 (9)	0 (0)
Invasion	9 (64)	4 (36)	8 (50)
Apoptosis/Necrosis <sup>†</sup>	12 (86)	7 (64)	8 (50)
Fibrosis	1 (7)	1 (9)	5 (31)
Angiogenesis	5 (36)	5 (45)	7 (44)

Significant at  $p < 0.05$ .

\*two-tailed.

<sup>†</sup>one-tailed Fisher's exact.

Many tumors showed multiple, mixed morphologies; therefore, the percentage reflects the proportion of tumors showing the phenotype within each genotype. We saw no differences due to the initial *p53* allele status (f/+ vs. f/f). We combined these classes ( $n = 11 + 16 = 27$ ) for statistical comparison to tumors with *Brca1* mutation ( $n = 14$ ).

doi:10.1371/journal.pgen.1003027.t001



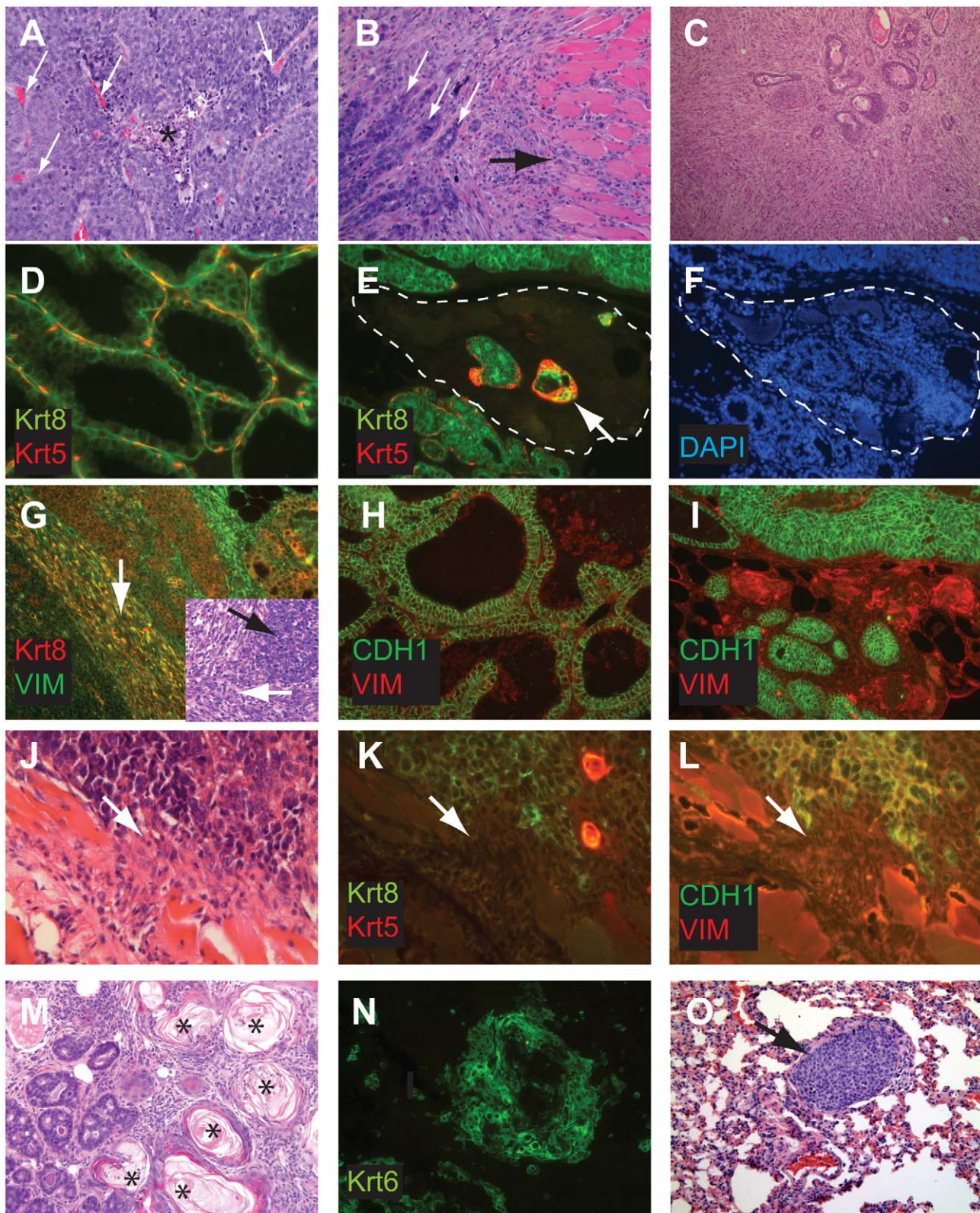


**Figure 4. Perturbed differentiation in TBP tumors.** Poorly differentiated tumors with solid morphology were most common (A), with and without vascularization (white arrows) or central necrosis (asterisk). Other tumors retained remnant glandular architecture (B, white arrows). Metaplastic cells invaded adjacent muscle and stroma (B, black arrow). Homogeneous spindloid cells of a carcinosarcoma entrap carcinomatous cells (C, 100 $\times$ ). Keratin-8 (Krt8, green) and Keratin-5 (Krt5, red) immunolabeling of luminal and myoepithelial cells, respectively (D, E, K). Greatly reduced expression of both Krt5 and Krt8 (E dashed lines, and K arrow). DAPI staining (blue) indicates the high cellularity of the region devoid of epithelial markers in panel E (F). Metaplastic tumor cells (G) with dual staining of Krt8 (red) and the mesenchymal marker Vimentin (green), or reduced Krt

staining (K). Abundant E-cadherin (CDH1, green) in normal adjacent (H) or well-differentiated tumor (I). Reduced or absent CDH1 along invasive tumor fronts (J–L). Keratinic whorls in squamous metaplastic cells (M, asterisks). Whorl-associated and disseminated Keratin 6 expression (N, green). Pulmonary metastases were observed in both  $T_{121}/p53$  and TBP mice (O, arrow). doi:10.1371/journal.pgen.1003027.g004

others that *Rb/p53* tumors can also resemble TNBC and the Claudin-low molecular phenotype [3,18,20]. A single TP tumor clustered among the previously designated Group II tumors (Figure 6A, yellow box), which are the paradigm cases of the Claudin-low subtype [3]. In addition, a single TP tumor clustered with tumors with a squamous metaplastic histology. Finally, two TP tumors co-segregated with the TBP tumors (Figure 6A, orange box), which is not surprising given that *Rb* is one of the most frequently deleted loci among *Brcal/p53*-mutated mouse tumors [22].

### Pathway analysis

The similarity between TBP tumors and human Claudin-low and Basal-like cancers was also evident from pathway analysis of up-regulated genes of each of the three tumor types (Figure 7A, File S1). We queried the KEGG (Kyoto Encyclopedia of Genes and Genomes) and GO (Gene Ontology) databases with lists of genes that were differentially expressed by TBP tumors (see Methods) and by human Claudin-low and Basal-like tumors [4]. Cytokine, chemokine, and MAPK signaling pathways ranked highly among both Claudin-low and TBP tumors. Pathways that are enriched in cancers of diverse origins ranked highly in both Basal-like and murine TBP tumors.

The GO terms associated with the respective tumor types were consistent with the enriched KEGG pathways. Cell-cycle progression (GO:0007049,  $p = 2.43551E-59$ ) and DNA repair (GO:0034984,  $p = 6.95081E-22$ ) dominate the list of functions enriched in Basal-like tumors (File S1). Similarly, regulation of cell proliferation (GO:0042127,  $p = 6.01E-13$ ) is among the top terms for TBP tumors. The three top scoring, inter-related GO terms for TBP tumors are regulation of developmental process (GO:0050793,  $p = 7.50E-16$ ), organ morphogenesis (GO:0009887,  $p = 3.53E-14$ ), and tissue development (GO:0009888,  $p = 1.36E-13$ ). These GO terms are reflective of the enrichment of the *Wnt*, *ErbB*, *TGF- $\beta$* , and *VEGF* signaling pathways identified by KEGG pathway analysis. Claudin-low tumors are enriched for wound (GO:0009611,  $p = 4.29939E-66$ ) and inflammatory responses (GO:0006954,  $p = 1.26817E-50$ ), which are also among the top functions associated with TBP tumors (7.37E-13 and 6.46E-12, respectively).

### CGH analysis

Given the requirement for *BRCA1* in DNA damage repair and centrosome regulation, we tested the hypothesis that TBP tumors harbor more genomic copy number aberrations (CNAs) than do TP tumors with intact *Brcal*. We enumerated CNAs by counting “copy number transitions,” the number of changes in the CGH profile from one copy number level to another that occur within chromosomes [34]. Unexpectedly, we found no statistically significant difference ( $p = 0.8374$ ) in the mean number of CNAs between TBP tumors ( $n = 8$ ) and TP tumors ( $n = 10$ ) using array-based comparative genomic hybridization (aCGH).

The low multiplicity of TBP and TP tumors (1–3 per mouse) and their latency indicate that combinations of *pRb*, *Brcal*, and *p53* pathway perturbations are not sufficient for malignant transformation in our models. To identify potentially collaborating oncogenic events, we manually curated loci with copy number changes (see Methods). In nine tumors (50%), we observed recurrent losses of large, variable regions spanning *chr4* and *chr10* (Figure 8). Both chromosomes harbor many potential tumor

suppressors, including regulators of cell death, such as *Tm2d1*, *Utp11l*, *Trp73*, *Dffa*, *Runx3*, *Lck*, *Dhcr24*, *Faf1*, *Pax7*, and *Casp9*, and effectors of cell death, such as *Col18a1*, *Gadd45b*, *Dapk3*, and *Casp14*. Among all the tumors assayed ( $n = 18$ ), we identified nearly five-hundred loci (Table S9 in File S1) with potential copy number gains. Approximately half of the genes are included on curated lists of cancer-associated genes, including the Cancer Gene Census (Sanger Institute) and the KEGG Pathways in Cancer. We observed focal amplification of several canonical proto-oncogenes, including *c-Myc* amplification ( $\log_2\text{ratio} = 3.64$ ,  $p < 0.0001$ ) in a single TP tumor, *H-ras* amplification in two of ten TP tumors, and *K-ras* amplification in two of eight TBP tumors. Pathway analysis of these five-hundred putative collaborating genes revealed enrichment of several signaling pathways, including the MAP Kinase, Focal Adhesion, Wnt, and ErbB pathways (Table S10 in File S1).

### Discussion

Here we report a highly penetrant engineered mouse model of TNBC. Our previous work showed that when *pRb* and *p53* are simultaneously perturbed in mammary epithelium, adenocarcinomas develop with long latency, suggesting a requirement for additional oncogenic events. However, these mouse tumors displayed only limited chromosomal copy number aberrations [19]. Because genomic instability is a hallmark of malignant transformation [35], especially among *BRCA1* familial cancers [36] and aggressive sporadic breast cancers [37], we hypothesized that *Brcal* mutation would accelerate the tumor development we observed following dual inactivation of *pRb* and *p53*. Our results show that concomitant inactivation of all three tumor suppressor pathways in mammary epithelium has an additive effect on tumor latency and predisposes highly penetrant, malignant carcinomas. Although *Brcal* inactivation accelerated tumorigenesis compared to TP tumors, we observed no statistical difference between chromosomal copy number transitions in tumors with or without *Brcal*, despite the extensive CNAs observed by others in *Brcal/p53* tumors [22].

The *pRb*-regulated cell cycle network is frequently disrupted in TNBC tumors [7,26,37,38], and the *Rb* locus is among the most frequently lost in *Brcal/p53* mouse tumors [22], indicating that there is strong selective pressure for *Rb* pathway inactivation. We speculate that direct inactivation of *pRb* by  $T_{121}$  may allow TBP cells to escape this rate-limiting barrier of transformation without accruing numerous chromosomal aberrations. Thus, in the context of defective *pRb* and *p53* function, tumor progression may be unrelated to the proportion of the genome altered by copy number alterations. It will be important to determine the effect of *Brcal* loss on the abundance and identities of somatic mutations that are not detectable by CGH.

The importance of *p53* mutation in breast cancers is well documented and is confirmed in the present study. The dual inactivation of *pRb* and *Brcal* caused markedly increased cell death that was reduced by *p53* mutation. *p53-independent* cell death likely remains a significant barrier to tumor progression among TBP tumors and may account, in part, for the observed loss of genomic regions that harbor cell death regulatory genes, most notably on *chr4* where the *p53* paralog *p73* resides. Identifying the genomic alterations that are conserved across species will be useful



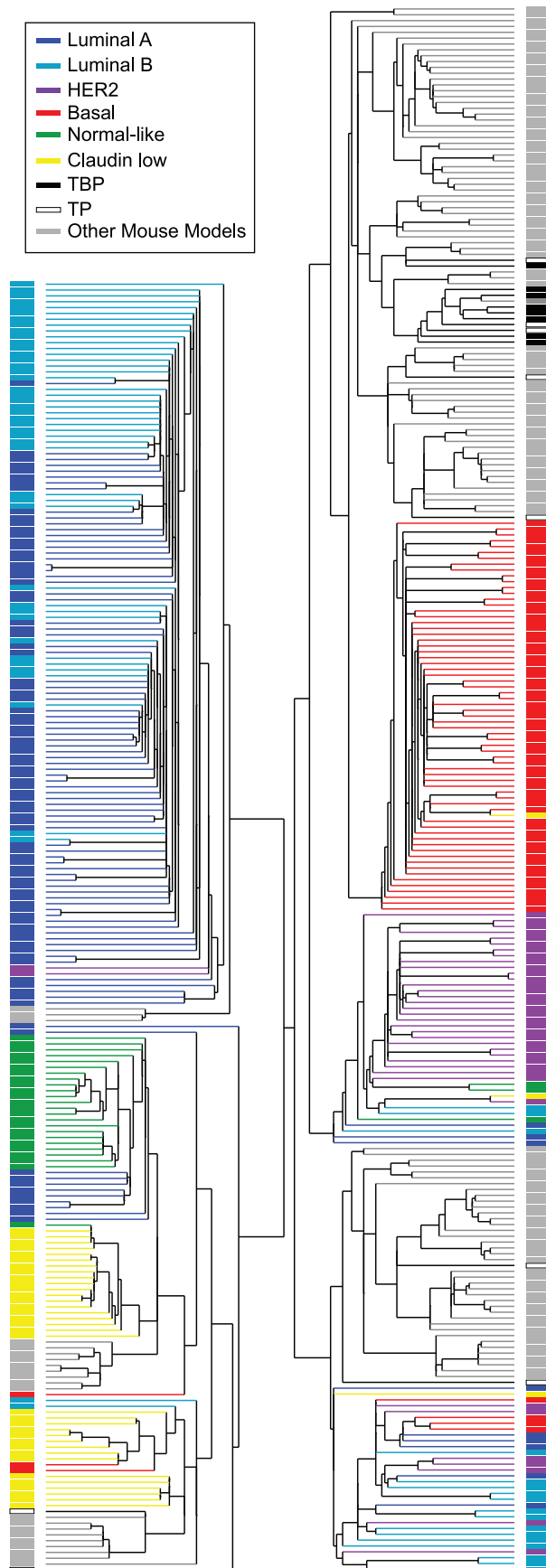


**Figure 5. Cross-species comparison of breast cancers.** TBP (black boxes,  $n=8$ ) and TP (open black boxes,  $n=9$ ) tumors were compared to published mouse (gray boxes,  $n=135$ ) and human ( $n=337$ ) microarray expression profiles (colored according to PAM50 subtype). Most (76%) of our *TgMFT*<sub>121</sub> mouse tumors cluster with human Basal-like breast cancers (red boxes). The Treeview files of the clustering analysis are available in File S2.  
doi:10.1371/journal.pgen.1003027.g005

in evaluating the impact of the myriad of CNAs observed in breast cancers and may help to explain the heterogeneity of TNBCs.

*Brca1* mutation not only accelerated tumor development but also shifted the tumor spectrum. Whereas *T*<sub>121</sub>/*p53* mouse tumors often resembled the Luminal-B molecular subtype breast cancers, which show relatively abundant expression of luminal epithelial cell differentiation markers, TBP tumors consistently shared features of Basal-like and Claudin-low molecular subtypes. Others have argued that Basal-like and Claudin-low gene expression signatures reflect progenitor and stem cell phenotypes, respectively [4,16], consistent with a role for *Brca1* in mediating stem/progenitor cell maturation [15]. Loss of BRCA1 activity may also alter tumor phenotype through deregulation of the EMT inducer SLUG [39].

The CGH analysis of our mouse tumors revealed CNAs consistent with mutations observed in genomic surveys of human breast cancers [40,41]. Similar to the studies of human tumors, we saw increased copy numbers of known oncogenic driver genes, including *myc*, *egfr*, *crebbp*, *jak1*, *H-ras*, and *K-ras*, as well as enrichment of pathways implicated in tumor progression, including the WNT signaling pathway, regulation of actin cytoskeleton, focal adhesion, cell shape, and mobility proteins. Far fewer investigations have focused on genetic deletions and cancer development mechanisms. We also found decreased copy numbers of known tumor suppressors, including *map2k*, *ppp2r*, and *pten*. Given the strong similarities between our mouse model and aggressive human breast cancers, the TBP model provides an invaluable preclinical platform to identify and assess potential therapeutics for aggressive and chemoresistant breast cancer subtypes [42,43].

## Materials and Methods

### Ethics statement

This study was performed in strict accordance with the recommendations in the Guide for the Care and Use of Laboratory Animals of the National Institutes of Health.

### Derivation of *MFT*<sub>121</sub> transgenic mice

The LoxP-eGFP-Stop-LoxP cassette and *T*<sub>121</sub>-encoding DNA were cloned into EcoRI HindIII sites of MMTV-SV40-Bssk (Addgene plasmid 1824). The LoxP-eGFP-Stop-LoxP cassette was provided courtesy of the T. Jacks lab. Resulting and subsequent generation *MFT*<sub>121</sub> transgenic mice were identified by PCR amplification of a 215-bp fragment using the oligo pair: 5'-GCATCCAGAAGCCTC-CAAAG-3' and 5'-GAATCTTTGCAGCTAATGGACC-3' complementary to the *T*<sub>121</sub> sequence. Cre transgenic mice were identified using the oligo pair: 5'-TGATGAGGTTCGCAAGAACC-3' and 5'-CCATGAGTGAACGAACCTGG-3'. The cycling profile was 94°C for 2 min., 35 cycles of 94°C for 20 sec., 62°C for 45 sec., and 72°C for 45 sec.; the final incubation of 72°C was for 2 min. We established five *TgMFT*<sub>121</sub> founder transgenic lines, though three lines failed to express the eGFP reporter. We describe here our studies of the single mouse line with higher eGFP expression in virgin mammary glands. eGFP expression was also evident in salivary glands and foot pads in this line (data not shown).

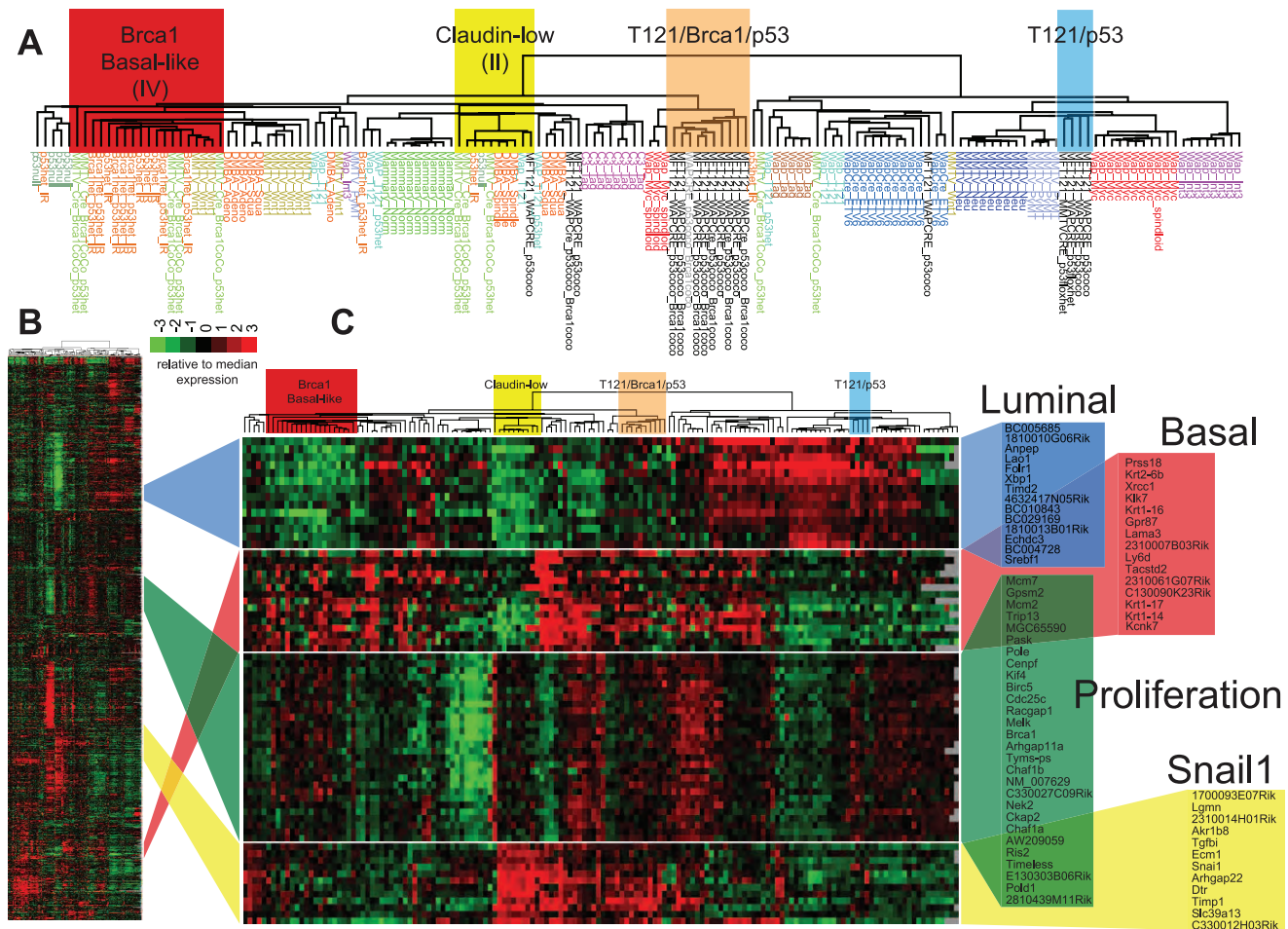


**Figure 6. TBP tumors share features of Basal-like and Claudin-low expression signatures.** (A) Expression of 866 reference genes of TP ( $n=9$ ) and TBP ( $n=8$ ) tumors and 13 models of breast cancer. Tumor annotations of the expanded dendrogram (A) are color coded by tumor model. Selected gene clusters (C) correspond to the full data matrix (B). TBP tumors (orange box) cluster with mouse tumors that more closely resemble TNBC on the left branch. 56% (5 of 9) of TP tumors clustered with Luminal-B tumors (blue box). TBP tumors show high expression of *Snail*-correlated genes in the Claudin-low cluster. The Treeview files of the clustering analysis are included in Table S1 in File S1. doi:10.1371/journal.pgen.1003027.g006

### Transgenic breeding strategies

*TgMFT<sub>121</sub>;TgWAP-Cre* mice were mated to *p53* conditional allele mice (*p53<sup>f/f</sup>*) [44]. *p53* genotypes were determined by PCR using two reactions: neomycin primer 5'-TCCTCGTGCTTTACGGTATC-3', *p53* primer 5'-TATACTCAGAGCCGGCCT-3', 525-bp product; the endogenous *p53* allele; substituting 5'-ACAGCGTGGTGG-TACCTTAT-3' for the *neo* primer, 475-bp product. Cycling parameters were the same as they were for the T<sub>121</sub> reaction. We produced female mice with the genotypes *TgMFT<sub>121</sub>;TgWAP-Cre;p53<sup>f/f</sup>* and *TgMFT<sub>121</sub>;TgWAP-Cre;p53<sup>f/f</sup>*, and female littermates served as controls. To study the effect of *Brca1* loss, *TgMFT<sub>121</sub>;TgWAP-Cre* mice were mated to *Brca1<sup>f/f</sup>;p53<sup>f/f</sup>* mice [44]. *Brca1* genotypes were determined by PCR using two reactions. We generated female mice with the genotypes *TgMFT<sub>121</sub>;TgWAP-Cre;Brca1<sup>f/f</sup>;p53<sup>f/f</sup>* and *TgMFT<sub>121</sub>;TgWAP-Cre;Brca1<sup>f/f</sup>;p53<sup>f/f</sup>* with nontransgenic (Cre negative) littermate controls for each cohort. Pregnancy induced *WAP-Cre* transgene expression. Parturition of the first litter was designated as Day 1 for all aging studies. Matings with *TgMMTV-Cre* mice (Line F) yielded small litter sizes; therefore, experiments reported here employed *TgWap-Cre* unless otherwise indicated.

### Histopathology and apoptosis assays

A portion of each mammary sample was fixed overnight in 10% phosphate-buffered formalin, transferred to 70% ethanol, and then embedded in paraffin. Samples were sectioned for 10 successive layers at 5- $\mu$ m intervals and stained with hematoxylin and eosin for histopathologic examination, as described previously. Apoptosis levels were assessed using the terminal deoxynucleotidyl transferase-mediated dUTP-biotin nick end labeling (TUNEL) method with standard protocols. Differences in apoptosis levels between mice with different genotypes were evaluated by the *t* test ( $p<0.05$  was deemed statistically significant).

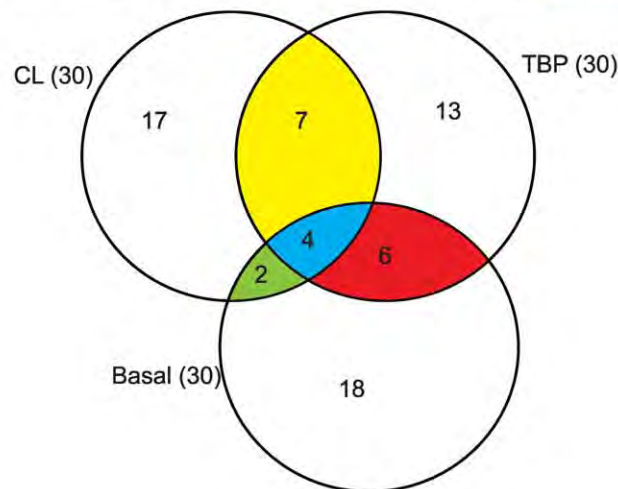
### Immunostaining

Immunohistochemical analysis was performed using formalin-fixed paraffin sections. Antigen retrieval for all antibodies was done by boiling the slides in citrate buffer (pH 6.0) for 15 min. Antibodies were  $\alpha$ -cytokeratins 8/18 (Ker8/18, 1:450 Progen, GP11),  $\alpha$ -cytokeratin 5 (K5, 1:8000, Covance, PRB-160P), smooth muscle actin (SMA; 1:1,000, mouse A2537; Sigma, St. Louis, MO), anti-phosphorylated histone H3 (1:100, rabbit 06-570; Upstate, Waltham, MA) and SV40



**A****Intersecting KEGG Pathway Terms (Top 30/tumor type)**

CL (human)		T121/Brca1/p53 (TBP, mouse)		Basal (human)	
KEGG Pathway (n=117)	adjpvalue	KEGG Pathway (n=71)	adjpvalue	KEGG Pathway (n=48)	adjpvalue
Cytokine-cytokine receptor interaction	5.38E-32	MAPK signaling pathway	9.86E-08	Cell cycle	1.06E-23
Chemokine signaling pathway	3.08E-28	Pathways in cancer	1.42E-07	Pathways in cancer	4.26E-11
Hematopoietic cell lineage	2.57E-25	Regulation of actin cytoskeleton	1.00E-06	DNA replication	1.61E-06
Cell adhesion molecules (CAMs)	1.24E-19	Focal adhesion	1.88E-05	p53 signaling pathway	3.92E-06
MAPK signaling pathway	1.82E-18	ECM-receptor interaction	1.88E-05	Homologous recombination	1.59E-05
Natural killer cell mediated cytotoxicity	3.33E-16	Fc gamma R-mediated phagocytosis	1.12E-04	Bladder cancer	5.78E-05
Pathways in cancer	1.15E-15	Cell adhesion molecules (CAMs)	2.24E-04	Purine metabolism	1.09E-04
Leukocyte transendothelial migration	5.68E-15	Leukocyte transendothelial migration	5.88E-04	Melanoma	1.27E-04
Jak-STAT signaling pathway	2.96E-14	Hematopoietic cell lineage	5.88E-04	Glioma	3.67E-04
Lysosome	1.43E-12	Adherens junction	8.53E-04	Oocyte meiosis	4.87E-04
Fc gamma R-mediated phagocytosis	1.67E-12	Colorectal cancer	9.71E-04	Pancreatic cancer	6.11E-04
T cell receptor signaling pathway	2.24E-12	Vascular smooth muscle contraction	9.71E-04	Fc gamma R-mediated phagocytosis	1.43E-03
Focal adhesion	7.53E-12	Wnt signaling pathway	1.47E-03	Progesterone-mediated oocyte maturation	1.99E-03
Graft-versus-host disease	4.91E-11	Melanoma	1.47E-03	Cysteine and methionine metabolism	2.07E-03
Complement and coagulation cascades	5.47E-11	Cytokine-cytokine receptor interaction	1.55E-03	Non-small cell lung cancer	2.73E-03
B cell receptor signaling pathway	8.26E-11	Glycosphingolipid biosynthesis - ganglio series	1.78E-03	Pyrimidine metabolism	2.73E-03
Neuroactive ligand-receptor interaction	9.73E-11	Non-small cell lung cancer	2.25E-03	Spliceosome	2.73E-03
PPAR signaling pathway	1.87E-10	GnRH signaling pathway	2.25E-03	Prostate cancer	3.01E-03
Viral myocarditis	5.47E-10	Bladder cancer	2.25E-03	Small cell lung cancer	3.04E-03
Calcium signaling pathway	5.59E-10	Glycosphingolipid biosynthesis - globo series	2.25E-03	Chronic myeloid leukemia	3.04E-03
NOD-like receptor signaling pathway	7.89E-10	Glioma	3.77E-03	Calcium signaling pathway	4.83E-03
Toll-like receptor signaling pathway	2.17E-09	ErbB signaling pathway	4.51E-03	Colorectal cancer	5.66E-03
Regulation of actin cytoskeleton	7.56E-09	TGF-beta signaling pathway	4.83E-03	Non-homologous end-joining	7.03E-03
Vascular smooth muscle contraction	1.01E-08	Chemokine signaling pathway	4.83E-03	Base excision repair	8.23E-03
mTOR signaling pathway	1.09E-08	Pancreatic cancer	5.43E-03	Mismatch repair	8.23E-03
Neurotrophin signaling pathway	1.12E-08	Endometrial cancer	5.44E-03	Regulation of actin cytoskeleton	8.28E-03
Primary immunodeficiency	2.17E-08	Arrhythmogenic right ventricular cardiomyopathy	5.47E-03	PPAR signaling pathway	8.74E-03
Allograft rejection	3.05E-08	VEGF signaling pathway	6.22E-03	Glycosphingolipid biosynthesis	1.29E-02
Fc epsilon RI signaling pathway	3.29E-08	Phosphatidylinositol signaling system	7.04E-03	One carbon pool by folate	1.30E-02
Type I diabetes mellitus	3.53E-08	Melanogenesis	8.22E-03	Focal adhesion	1.51E-02

**B**

**Figure 7. Intersecting KEGG pathway terms.** (A) The genes differentially expressed among mouse TBP tumors show enrichment of KEGG pathways associated with human Claudin-low and Basal-like tumors. (B) The pathway terms are colored according to the intersections depicted in the Venn diagram. The full KEGG pathway lists are included in Table S1 in File S1.  
doi:10.1371/journal.pgen.1003027.g007

(monoclonal Ab2, 1:100; Oncogene, Cambridge, MA). All immunofluorescence reactions were done using AlexaFluor-conjugated secondary antibodies (AlexaFluor 488 and 594, Molecular Probes). Slides were counterstained with 4',6-diamidino-2-phenylindole (DAPI) using Hardset Mounting Media (Vector Laboratories).

**Microarray analysis**

We compared microarray profiles of T<sub>121</sub>/p53 (n = 9) and TBP (n = 8) tumors to published microarray profiles (n = 152) using two-way hierarchical clustering (centroid linkage) of 866 “intrinsic genes” [3,45]. Total RNA was collected from end-stage tumors.



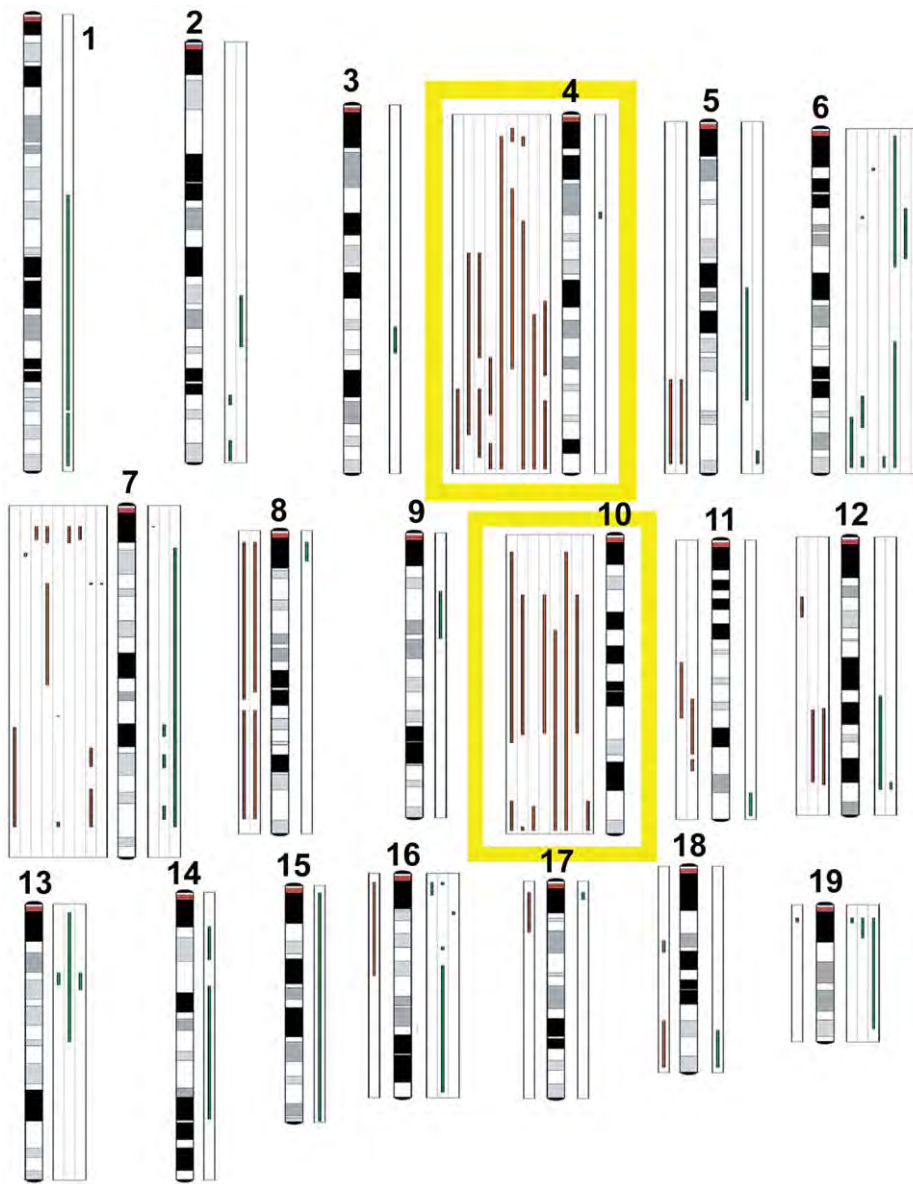


**Figure 8. Comparative genomic hybridization.** TBP tumors ( $n = 8$ ) and TP tumors ( $n = 10$ ) were analyzed by array CGH to identify copy number aberrations (CNAs). Green lines to the right of the chromosome ideograms indicate gains and red lines to the left indicate losses of individual tumor samples. No significant difference was found between the average number of CNAs between TBP and TP tumors ( $p = 0.8374$ ). Frequent losses were seen on chromosomes 4 and 10. Other recurrent losses included chromosome 7. Frequent gains were associated with chromosome 6. doi:10.1371/journal.pgen.1003027.g008

RNA was purified using the Qiagen RNeasy Mini Kit according to the manufacturer's protocol using 20–30 mg tissue. RNA integrity was assessed using the RNA 6000 Nano LabChip by Bioanalyzer (Agilent). Two micrograms of total RNA were reverse transcribed, amplified, and labeled with Cy5 using a Low RNA Input Amplification kit (Agilent). Common reference RNA consisted of total RNA harvested from equal numbers of C57Bl6/J and 129 male and female Day 1 pups (courtesy of Dr. Cam Patterson, UNC). Reference RNA was reverse transcribed, amplified, and labeled with Cy3. The amplified sample and reference were co-hybridized overnight to Agilent Mouse Oligo Microarrays (G4121A). They were then washed and scanned on an Axon GenePix 4000B scanner, analyzed using GenePix 4.1 software, and uploaded into the UMD database (<https://genome.unc.edu/>) where Lowess normalization is automatically performed. All data were submitted

to GEO (GSE34479). The genes for all analyses were filtered by: 1) requiring intensity values in both channels to have a mean Lowess normalized intensity of  $>10$ , 2) Values being reported in  $>70\%$  of the samples, and 3) the absolute value of the  $\log_2$  of the ratio of Channel 2/Channel 1 for at least three arrays having to be  $>1.6$ . Hierarchical clustering was performed using Cluster v3.0 and displayed using JavaTreeview v1.0.8.

We identified 871 differentially expressed TBP transcripts using SAM implemented in BRB-ArrayTools (R. Simon and the BRB-ArrayTools Development Team, NCI; Table 1; FDR 0.0485, delta 0.92931). Gene ontology analyses were performed using the FatiGO tool (Babelomics ver. 4.2, [babelomics.bioinfo.cipf.es](http://babelomics.bioinfo.cipf.es)). Mouse gene symbols were converted to human EntrezIDs using Agilent annotations and the Mouse Genome Informatics database of The Jackson Laboratory for comparisons. The Fisher's exact

two-tailed test was used to determine significance of GO (biological process [levels 3–9]) and KEGG pathway terms. Terms with  $p < 0.05$  are reported.

### Combined murine and human expression data sets

For the mouse tumor data set, IDs for 21,670 unfiltered probes were retrieved (GSE34479). Human EntrezIDs were assigned to orthologous genes as above. Mean values of redundant mouse probes were calculated, missing values were imputed, the columns were standardized to  $N(0,1)$ , and the rows were median centered using R (ver. 2.10.0). For the human data set, we downloaded the file “UNC337arraydata\_imputedCollapsed.txt” [4] from the UNC MicroArray Database (genome.unc.edu). The two data sets were corrected for systemic biases using Distance Weighted Discrimination [46]. The combined data set was used for centroid linkage hierarchical clustering analysis.

### CGH analysis

We performed array CGH essentially as previously described [47]. Briefly, genomic DNA was isolated from tumors, fluorescently labeled, and competitively hybridized with wt DNA spotted BAC (Bacterial Artificial Chromosomes) arrays. All data were submitted to GEO (GSE40925). We used the HaarSeg algorithm with default parameters implemented in waviCGH (wavi.bioinfo.cnio.es) for chromosomal segmentation of mutations and for CNA calling. We manually curated BAC clones spanning putative CNAs with a conservative tumor:normal DNA threshold of  $\log_2\text{ratio} > 0.5$  or  $< -0.5$ . Genes mapping to the BAC clones were identified using the National Center for Biotechnology Map Viewer and the Jackson Laboratory Mouse Genome Database. Gene lists were compared to the Cancer Gene Census (Sanger Institute), the KEGG Pathways in Cancer, Atlas Genetics Oncology, and the Michigan Molecular Interactions database. For the pathway analysis, we used the SAM algorithm implemented in BRB-Array Tools to identify differentially expressed genes (**TBP\_SAM**) among TBP tumors versus the rest of the mouse tumors in the data set. We interrogated KEGG (**TBP\_KEGG**) and GO (**TBP\_GO\_BP**) databases using the FatiGO algorithm implemented in the Babelomics (ver. 4.2) suite of bioinformatics tools (babelomics.bioinfo.cipf.es). We compared these results to the differentially expressed genes reported by Prat et al. (2010) of human Claudin-low (**CL\_KEGG**, **CL\_GO\_BP**) and Basal-like (**Basa\_KEGG**, **Basal\_GO\_BP**) tumors. We also used the FatiGO tool in the Babelomics 4.3.0 integrative platform with parameters set for the Fisher's exact two-tailed test to

determine the most alternately expressed KEGG pathways among the amplified genes determined by CGH analysis.

### Supporting Information

**Figure S1** Hierarchical clustering of the cross-species analysis summarized in Figure 5.

(PDF)

**File S1** Tumor annotations (Table S1 Tumor\_Descriptors). Differentially expressed genes defined by SAM analysis of TBP tumors (S2 TBP\_SAM). Gene Ontology (GO) terms enriched among tumor TBP, Basal, and Claudin-low subtypes (S3 TBP\_GO\_BP, S4 Basal\_GO\_BP, and S5 CL\_GO\_BP). KEGG pathways enriched among the tumor subtypes (S6 TBP\_KEGG, S7 Basal\_KEGG, S8 CL\_KEGG). Among all tumors assayed ( $n = 18$ ), we identified nearly five-hundred loci with potential copy-number gains ( $\log_2\text{ratio} > 0.5$ , Table S9 putative\_gained\_CGH\_loci). Approximately half of the genes are previously defined oncogenes represented in oncogene lists including the Cancer Gene Census (Sanger Institute) and the KEGG Pathways in Cancer. The KEGG Pathways enriched among putative gained genes (Table S10 CGH\_Gain\_KEGG).

(XLSX)

**File S2** JavaTreeview data files of the cross-species clustering analysis shown in Figure 5.

(ZIP)

**File S3** JavaTreeview data files of the mouse tumor clustering analysis shown in Figure 6.

(ZIP)

### Acknowledgments

This manuscript is dedicated to the memories of our colleagues R. Thresher and A. Wolthausen. Expert technical assistance was provided by H. Wu, D. Fogarty, C. Yang, L. Lu, D. Roth, A. Agrawal, and M. Zayed. We thank X. Lu for critically reading the manuscript and J. Jonkers for helpful discussions. We also extend special thanks to N. Ekross and Dr. S. Gupta.

### Author Contributions

Conceived and designed the experiments: PK MM KS. Performed the experiments: PK MM MP KS. Analyzed the data: PK MM JPSJ KS. Contributed reagents/materials/analysis tools: PK KS DGA BH. Wrote the paper: JPSJ KS.

### References

- Carey L, Winer E, Viale G, Cameron D, Gianni L. (2010) Triple-negative breast cancer: Disease entity or title of convenience? *Nat Rev Clin Oncol* 7(12): 683–692.
- Rakha EA, El-Sayed ME, Reis-Filho J, Ellis IO. (2009) Patho-biological aspects of basal-like breast cancer. *Breast Cancer Res Treat* 113(3): 411–422.
- Herschkowitz JI, Simin K, Weigman VJ, Mikaelian I, Usary J, et al. (2007) Identification of conserved gene expression features between murine mammary carcinoma models and human breast tumors. *Genome Biol* 8(5): R76.
- Prat A, Parker JS, Karginova O, Fan C, Livasy C, et al. (2010) Phenotypic and molecular characterization of the claudin-low intrinsic subtype of breast cancer. *Breast Cancer Res* 12(5): R68.
- Liedtke C, Mazouni C, Hess KR, Andre F, Tordai A, et al. (2008) Response to neoadjuvant therapy and long-term survival in patients with triple-negative breast cancer. *J Clin Oncol* 26(8): 1275–1281.
- Carey LA, Dees EC, Sawyer L, Gatti L, Moore DT, et al. (2007) The triple negative paradox: Primary tumor chemosensitivity of breast cancer subtypes. *Clin Cancer Res* 13(8): 2329–2334.
- Herschkowitz JI, He X, Fan C, Perou CM. (2008) The functional loss of the retinoblastoma tumour suppressor is a common event in basal-like and luminal B breast carcinomas. *Breast Cancer Res* 10(5): R75.
- Sorlie T, Perou CM, Tibshirani R, Aas T, Geisler S, et al. (2001) Gene expression patterns of breast carcinomas distinguish tumor subclasses with clinical implications. *Proc Natl Acad Sci U S A* 98(19): 10869–10874.
- Sorlie T, Tibshirani R, Parker J, Hastie T, Marron JS, et al. (2003) Repeated observation of breast tumor subtypes in independent gene expression data sets. *Proc Natl Acad Sci U S A* 100(14): 8418–8423.
- Borresen-Dale AL. (2003) TP53 and breast cancer. *Hum Mutat* 21(3): 292–300.
- Schuyler M, Berns EM. (1999) Is TP53 dysfunction required for BRCA1-associated carcinogenesis? *Mol Cell Endocrinol* 155(1–2): 143–152.
- Esteller M, Silva JM, Dominguez G, Bonilla F, Matias-Guix X, et al. (2000) Promoter hypermethylation and BRCA1 inactivation in sporadic breast and ovarian tumors. *J Natl Cancer Inst* 92(7): 564–569.
- Walsh T, King MC. (2007) Ten genes for inherited breast cancer. *Cancer Cell* 11(2): 103–105.
- Welsh PL, Lee MK, Gonzalez-Hernandez RM, Black DJ, Mahadevappa M, et al. (2002) BRCA1 transcriptionally regulates genes involved in breast tumorigenesis. *Proc Natl Acad Sci U S A* 99(11): 7560–7565.
- Liu S, Ginestier C, Charafe-Jauffret E, Foco H, Kleer CG, et al. (2008) BRCA1 regulates human mammary stem/progenitor cell fate. *Proc Natl Acad Sci U S A* 105(5): 1680–1685.

16. Lim E, Vaillant F, Wu D, Forrest NC, Pal B, et al. (2009) Aberrant luminal progenitors as the candidate target population for basal tumor development in BRCA1 mutation carriers. *Nat Med* 15(8): 907–913.
17. Drost RM, Jonkers J. (2009) Preclinical mouse models for BRCA1-associated breast cancer. *Br J Cancer* 101(10): 1651–1657.
18. Cheng L, Zhou Z, Flesken-Nikitin A, Toshkov IA, Wang W, et al. (2010) Rb inactivation accelerates neoplastic growth and substitutes for recurrent amplification of cIAP1, cIAP2 and Yap1 in sporadic mammary carcinoma associated with p53 deficiency. *Oncogene* 29(42): 5700–5711.
19. Simin K, Wu H, Lu L, Pinkel D, Albertson D, et al. (2004) pRb inactivation in mammary cells reveals common mechanisms for tumor initiation and progression in divergent epithelia. *PLoS Biol* 2: e22. doi:10.1371/journal.pcbi.0010022
20. Jiang Z, Deng T, Jones R, Li H, Herschkowitz JI, et al. (2010) Rb deletion in mouse mammary progenitors induces luminal-B or basal-like/EMT tumor subtypes depending on p53 status. *J Clin Invest* 120(9): 3296–3309.
21. Lu X, Yang C, Yin C, Van Dyke T, Simin KJ. (2011) Apoptosis is the essential tumor suppression function of p53 during carcinoma progression. *Mol Cancer Res*.
22. Holstege H, van Beers E, Velds A, Liu X, Joosse SA, et al. (2010) Cross-species comparison of aCGH data from mouse and human BRCA1- and BRCA2-mutated breast cancers. *BMC Cancer* 10: 455.
23. Scambia G, Lovergine S, Masciullo V. (2006) RB family members as predictive and prognostic factors in human cancer. *Oncogene* 25(38): 5302–5308.
24. Ertel A, Dean JL, Rui H, Liu C, Witkiewicz AK, et al. (2010) RB-pathway disruption in breast cancer: Differential association with disease subtypes, disease-specific prognosis and therapeutic response. *Cell Cycle* 9(20): 4153–4163.
25. Bieche I, Lidereau R. (2000) Loss of heterozygosity at 13q14 correlates with RB1 gene underexpression in human breast cancer. *Mol Carcinog* 29(3): 151–158.
26. Shah SP, Roth A, Goya R, Oloumi A, Ha G, et al. (2012) The clonal and mutational evolution spectrum of primary triple-negative breast cancers. *Nature*.
27. Simin K, Hill R, Song Y, Zhang Q, Bash R, et al. (2005) Deciphering cancer complexities in genetically engineered mice. *Cold Spring Harb Symp Quant Biol* 70: 283–290.
28. Wagner KU, Wall RJ, St-Onge L, Gruss P, Wynshaw-Boris A, et al. (1997) Cre-mediated gene deletion in the mammary gland. *Nucleic Acids Res* 25(21): 4323–4330.
29. Clark-Knowles KV, Senterman MK, Collins O, Vanderhyden BC. (2009) Conditional inactivation of Brca1, p53 and rb in mouse ovaries results in the development of leiomyosarcomas. *PLoS ONE* 4: e8534. doi:10.1371/journal.pone.0008534
30. Jonkers J. (2001) Synergistic tumor suppressor activity of BRCA2 and p53 in a conditional mouse model for breast cancer. *Nature Genetics* 29(4): 418.
31. Xiao A, Wu H, Pandolfi PP, Louis DN, Van Dyke T. (2002) Astrocyte inactivation of the pRb pathway predisposes mice to malignant astrocytoma development that is accelerated by PTEN mutation. *Cancer Cell* 1(2): 157–168.
32. Jerry DJ, Kuperwasser C, Downing SR, Pinkas J, He C, et al. (1998) Delayed involution of the mammary epithelium in BALB/c-p53null mice. *Oncogene* 17(18): 2305–2312.
33. Cardiff RD. (2010) The pathology of EMT in mouse mammary tumorigenesis. *J Mammary Gland Biol Neoplasia* 15(2): 225–233.
34. Snijders AM, Fridlyand J, Mans DA, Segreaves R, Jain AN, et al. (2003) Shaping of tumor and drug-resistant genomes by instability and selection. *Oncogene* 22(28): 4370–4379.
35. Hanahan D, Weinberg RA. (2011) Hallmarks of cancer: The next generation. *Cell* 144(5): 646–674.
36. Jonsson G, Naylor TL, Vallon-Christersson J, Staaf J, Huang J, et al. (2005) Distinct genomic profiles in hereditary breast tumors identified by array-based comparative genomic hybridization. *Cancer Res* 65(17): 7612–7621.
37. Fridlyand J, Snijders A, Ylstra B, Li H, Olshen A, et al. (2006) Breast tumor copy number aberration phenotypes and genomic instability. *BMC Cancer* 6(1): 96.
38. Gauthier ML, Berman HK, Miller C, Kozakeiwicz K, Chew K, et al. (2007) Abrogated response to cellular stress identifies DCIS associated with subsequent tumor events and defines basal-like breast tumors. *Cancer Cell* 12(5): 479–491.
39. Proia TA, Keller PJ, Gupta PB, Klebba I, Jones AD, et al. (2011) Genetic predisposition directs breast cancer phenotype by dictating progenitor cell fate. *Cell Stem Cell* 8(2): 149–163.
40. Curtis C, Shah SP, Chin SF, Turashvili G, Rueda OM, et al. (2012) The genomic and transcriptomic architecture of 2,000 breast tumours reveals novel subgroups. *Nature* 486(7403): 346–352.
41. Chin K, DeVries S, Fridlyand J, Spellman PT, Roydasgupta R, et al. (2006) Genomic and transcriptional aberrations linked to breast cancer pathophysiology. *Cancer Cell* 10(6): 529–541.
42. Hennessey BT, Gonzalez-Angulo AM, Stemke-Hale K, Gilcrease MZ, Krishnamurthy S, et al. (2009) Characterization of a naturally occurring breast cancer subset enriched in epithelial-to-mesenchymal transition and stem cell characteristics. *Cancer Res* 69(10): 4116–4124.
43. Taube JH, Herschkowitz JI, Komurov K, Zhou AY, Gupta S, et al. (2010) Core epithelial-to-mesenchymal transition interactome gene-expression signature is associated with claudin-low and metaplastic breast cancer subtypes. *Proc Natl Acad Sci U S A* 107(35): 15449–15454.
44. Liu X, Holstege H, van der Gulden H, Treur-Mulder M, Zevenhoven J, et al. (2007) Somatic loss of BRCA1 and p53 in mice induces mammary tumors with features of human BRCA1-mutated basal-like breast cancer. *Proc Natl Acad Sci U S A* 104(29): 12111–12116.
45. Li Z, Tognon CE, Godinho FJ, Yasaitis L, Hock H, et al. (2007) ETV6-NTRK3 fusion oncogene initiates breast cancer from committed mammary progenitors via activation of AP1 complex. *Cancer Cell* 12(6): 542–558.
46. Benito M, Parker J, Du Q, Wu J, Xiang D, et al. (2004) Adjustment of systematic microarray data biases. *Bioinformatics* 20(1): 105–114.
47. Snijders AM, Nowak NJ, Huey B, Fridlyand J, Law S, et al. (2005) Mapping segmental and sequence variations among laboratory mice using BAC array CGH. *Genome Res* 15(2): 302–311.

**S A Jansen<sup>1</sup>, L Ileva<sup>2</sup>, L Riffle<sup>2</sup>, L Lu<sup>1</sup>, M Anver<sup>3</sup>, J D Kalen<sup>2</sup> and T Van Dyke<sup>1¶</sup>.**

<sup>3</sup>Pathology/Histotechnology Laboratory, SAIC-Frederick, Frederick National Laboratory for Cancer Research

Device Type	Percentage of Respondents
Smartphone	85%
Tablet	65%
Smartwatch	45%
Smart TV	35%
Smart Home Assistant	30%
Smart Car	25%
Smart Thermostat	20%
Smart Light Bulbs	15%
Smart Door Lock	10%
Smart Security Camera	5%

## ABSTRACT

The earliest stage of breast cancer, ductal carcinoma *in situ* (DCIS), is a remarkably heterogeneous disease with diverse molecular and prognostic subtypes. Mouse models of breast cancer offer an effective experimental framework in which to investigate DCIS, and biomedical imaging can provide potential insights into the biology of these models. In this study, we develop a high resolution, multi-modality strategy for imaging preinvasive mammary neoplasias in two mouse models of DCIS. We performed high resolution magnetic resonance imaging (MRI) on a 3Tesla clinical scanner, using noncontrast T<sub>1</sub> and T<sub>2</sub> weighted acquisitions and dynamic contrast enhanced MRI. Preinvasive lesions were readily identified on noncontrast T<sub>1</sub> and T<sub>2</sub> weighted acquisitions. Subsequently, MRI-directed ultrasound was performed and an agar grid was used to correlate MRI with ultrasound and histology. We found that both MRI and ultrasound were able to detect preinvasive neoplasias with high sensitivity (over 90% in the posterior inguinal mammary glands). This study has established an imaging strategy for monitoring mouse models of DCIS, with rapid imaging acquisitions in two different modalities. We have also introduced a new method for correlating MRI with ultrasound and histology. This work sets the stage for combining advanced imaging and mouse modeling techniques to gain relevant insights on image-based biomarkers of DCIS.

**Keywords:** DCIS, breast cancer, MRI, ultrasound, mouse models



## INTRODUCTION

Ductal carcinoma *in situ* (DCIS) is a preinvasive breast cancer wherein neoplastic cells remain confined within the milk duct basement membrane. DCIS is a nonobligate precursor to invasive ductal carcinoma (IDC) and comprises 20-30% of newly diagnosed breast cancers in the US (Kerlikowske, 2010). It is a remarkably heterogeneous disease with distinct histological and molecular subtypes. These include nuclear grade (low, intermediate or high), gene-expression profiling patterns (luminal A, luminal B, basal or ERBB2) and alterations in regulators of cellular proliferation, apoptosis and genomic stability such as HER2, Rb and PTEN (Allred, 2010, Lari and Kuerer, 2011). Perhaps most relevant are the subtypes of DCIS with more aggressive growth, i.e., lesions that differentiate based on risk of progression to invasive carcinoma (Allegra et al., 2010). Indirect evidence suggests that a significant portion of DCIS lesions will never progress to an invasive, life-threatening carcinoma (Erbas et al., 2006). However, reliable identification of this subset of women with indolent disease who may benefit from less aggressive therapeutic interventions is not currently possible based on known histological or molecular characteristics (Allegra et al., 2010).

As a complementary approach, the capacity for *in vivo* imaging to provide a noninvasive characterization of DCIS biological and physical properties is an important goal (Jansen, 2011). Clinically, DCIS presents as calcifications on x-ray mammography in a variety of shapes and distributions (D'Orsi, 2010). On dynamic contrast enhanced MRI (DCEMRI) DCIS exhibits a distinctive nonmass-like morphology, with a diversity of distributions and internal enhancement patterns as described by the Breast Imaging and Reporting Data System (BIRADS) lexicon (Jansen et al., 2007). The contrast media uptake and washout, or kinetic, curves for DCIS usually exhibit a plateau or washout shape (Jansen et al., 2007). Breast ultrasound is a widely performed clinical imaging technique, most often utilized in a mammogram- or MRI-directed manner to further evaluate detected abnormalities (Abe et al., 2010). DCIS typically presents as a hypoechoic lesion with irregular shape and indistinct margins on ultrasound (Cho et al., 2011). Despite the widespread use of imaging in the management of DCIS, the association between image-based features and the underlying molecular and prognostic subtypes of DCIS is not well

understood. Studies of women with DCIS are hampered by several challenges including applying consistent imaging techniques in large cohorts of women, obtaining access to tissue specimens, and performing accurate radiologic-pathologic correlation.

Mouse models provide an appealing alternative experimental framework for investigating image-based biomarkers of DCIS because they, in principle, do not suffer from these limitations. As a further advantage, in genetically engineered mouse models (GEMMs), distinct genetic alterations can be targeted to the mammary epithelium in an experimentally controlled manner. These, in turn, have the potential to generate different molecular and prognostic subtypes of preinvasive cancer that can form the foundation for investigating imaging correlations (Van Dyke and Jacks, 2002). However, if mouse models are to serve as a test-bed for developing image-based molecular and prognostic biomarkers of DCIS, several technical advances are required. First, for the purpose of studying molecular, metabolic or physical imaging signatures, highly sensitive anatomic imaging techniques are essential for accurate lesion detection and localization. Second, it is critical to develop multimodality co-registration techniques that can register images with one another and with histology. In this study, we set out to address these goals. We have developed and validated an MRI and ultrasound imaging approach for characterizing preinvasive neoplasias in two mouse models of DCIS.

## MATERIALS AND METHODS

### Animals

All procedures were carried out in accordance with our institution's Animal Care and Use Committee approval. Twenty-two mice from commonly utilized xenograft (n=5) and GEMM (n=17) models of DCIS were selected. In MCF10DCIS xenograft mice, human cells were injected into the inguinal mammary gland #4 of 8-10 week old athymic nude mice and DCIS-like lesions developed after ~3 weeks (Miller et al., 2000, Hu et al., 2008). In the C3(1) SV40 Tag GEMM, mammary intraepithelial neoplasia (MIN), an analog to human DCIS, developed at ~12 weeks of age while invasive ductal carcinoma developed by ~16 weeks of age (Green et al., 2000, Maroulakou et al., 1994). Animals were anesthetized prior to imaging experiments, and anesthesia was maintained during imaging at 1.5% isoflurane. The temperature, heart rate and respiration rate were monitored with data taken every minute, and the respiration rate was used to obtain gated images when necessary. All four inguinal mammary glands were imaged, numbered #4,5 (left side), and #9,10 (right side). Glands #4 and #9 extend from the intramammary lymph node to the spine, and will be referred to as the *posterior inguinal* glands. Glands #5 and #10 extend down the belly of the animal, and will be referred to as the *anterior inguinal* glands (Figure 1).

### Imaging protocols and co-registration

The experimental workflow is illustrated in Figure 1, consisting of preparation and placement of the agar grid, MRI, MRI-directed ultrasound, and euthanization for subsequent tissue processing and histological evaluation.

*Agar grid:* A fine polyethylene mesh ~ 65 mm × 30 mm in size with 3 mm spacing was embedded in partially deuterated agar and wrapped around each mouse during imaging. Using Sharpie markers, the grid edges were marked on the skin of the mouse. In prior work, this grid has been shown to produce a two-dimensional coordinate system on MRI that allows for correlation with histology (Jansen et al., 2008)

and for registration of serial MRI scans (Jansen et al., 2009a). In the present study, the agar grid was used to co-register MRI with ultrasound and histology.

*MRI protocols:* Imaging was performed on a 3.0T Philips Achieva scanner. Mice were positioned in a volume coil so that the inguinal intramammary lymph nodes were in the center of the coil. Initially, a T<sub>1</sub> weighted acquisition with fat suppression was performed (T<sub>1</sub> FFE, 3D, TR/TE 26/2.9ms, in plane resolution=0.2 mm, slice thickness=0.4 mm, field of view (FOV)=30×20×9 mm, number of excitations (NEX)=8, flip angle (FA)=25°, no respiratory gating) followed by a T<sub>2</sub> weighted scan with fat suppression (T<sub>2</sub> TSE, 2D, TR/TE=4000/65 ms, in plane resolution = 0.17 mm, slice thickness=0.5 mm, FOV=30×30×12 mm, NEX=2, number of slices =24, with respiratory gating). On a subset of n=9 C3(1) SV40 Tag mice, dynamic contrast enhanced MRI (DCEMRI) (T<sub>1</sub> FFE DCE, 3D, TR/TE=13/3ms, in plane resolution =0.23 mm, slice thickness=1.0 mm, NEX=2, FA=20°, temporal resolution= 17 secs, duration =17 min 42 sec, no respiratory gating) was obtained before, during and after a single-dose injection of gadopentetate dimeglumine (Magnevist; Berlex, Wayne, NJ) via a tail vein catheter at a dose of 0.2 mmol/kg.

*MRI-directed ultrasound:* Ultrasound was subsequently performed to further evaluate MR findings. To correlate MRI and ultrasound, the grid coordinates of MRI-detected lesions were noted on the MRI, and then transferred to the skin of the mouse (Figure 1). These skin markings were subsequently used to guide placement of a 40 MHz ultrasound transducer for the acquisition of B-mode images on a Vevo2100 imaging system (VisualSonics Inc, Toronto Canada).

### **Correlation of MRI with histology**

To evaluate the sensitivity of MRI and ultrasound methods for detecting preinvasive lesions, hematoxylin and eosin (H&E) stained sections of imaged mammary glands were obtained (5-micron thick H&E sections every 50 microns) and evaluated by a veterinary pathologist (MA). Each gland (#4,5,9,10) was separately classified into one of four categories: (i) normal, (ii) preinvasive carcinoma with/without microinvasion, (iii) invasive and preinvasive carcinoma, and (iv) predominantly invasive carcinoma. MR

images were reviewed by a post-doctoral fellow (SAJ) with 6 years of experience analyzing MRI of the mouse mammary gland, and each gland (#4,5,9,10) was classified into the same categories, using the morphologic descriptors *nonmass* and *mass* to identify preinvasive and invasive regions, respectively (Jansen et al., 2009a, Jansen et al., 2008). The MRI assessment was blinded to the pathological assessment. MR images were spatially correlated with H&E sections using the agar grid as detailed in prior work (Jansen et al., 2008) and the sensitivity of MRI was calculated using the histologic evaluation as the reference standard. Sensitivity was compared in the posterior and anterior inguinal glands to determine regional variability in the efficacy of MRI.

### Image Analysis

*mBIRADS*: T<sub>1</sub> FFE images were analyzed according to an adapted version of the human BIRADS lexicon (ACR, 2003), referred to as the mouse BIRADS or mBIRADS lexicon. Initially the *type* of the lesion was classified as ‘mass’ or ‘nonmass’. Prior work has shown that the ‘nonmass’ descriptor reliably identifies preinvasive lesions in the C3(1) SV40 Tag model (Jansen et al., 2008). For nonmass lesions, additional descriptors were the *distribution* (‘linear’, ‘ductal’ or ‘segmental’) and the *pattern* (‘homogeneous’, ‘clumped’ or ‘stippled’).

*SNR and CNR*. All data analysis was performed using software written in IDL (Research Systems, Inc., Boulder, CO, USA). A postdoctoral fellow (SAJ) with six years of experience analyzing MRI of preinvasive and invasive mammary cancers traced the following regions of interest (ROI), confirmed by the histologic evaluation: invasive carcinoma, preinvasive carcinoma, lymph node, normal mammary gland (NMG) and muscle. The signal-to-noise ratio (SNR) and the contrast-to-noise ratio (CNR) relative to NMG tissue and muscle were calculated on T<sub>1</sub> FFE and T<sub>2</sub> TSE as follows:

$$SNR = \bar{S} / \sigma_{noise} \quad CNR_{NMG} = SNR_{ROI} - SNR_{NMG} \quad CNR_{muscle} = SNR_{ROI} - SNR_{muscle}$$

where  $\bar{S}$  is the average signal intensity in the ROI and  $\sigma_{noise}$  was averaged from the standard deviations of signal intensities measured in a 5×5 mm ROI drawn in the corners of the image.



*Contrast kinetics.* Signal intensity vs. time, or kinetic, curves were generated from T<sub>1</sub> FFE DCE data by manually tracing an ROI around lesions. These curves were analyzed qualitatively and classified as persistent, plateau or washout as described by the BIRADS lexicon (ACR, 2003). In addition, two compartment pharmacokinetic modeling was performed and parameters  $K^{\text{trans}}$  and  $v_e$  calculated, using software as described previously (Turkbey et al., 2010).

### **Statistical analysis**

The SNR, CNR<sub>NMG</sub> and CNR<sub>muscle</sub> of lymph nodes, invasive and preinvasive carcinomas on T<sub>1</sub> FFE and T<sub>2</sub> TSE pulse sequences were compared using the Student's *t*-test. The sensitivity of MRI and MRI-directed ultrasound in the posterior vs. anterior inguinal glands was compared using the Fishers exact test. For both tests, a *p* value < 0.05 was considered to be statistically significant.

## RESULTS

Images of preinvasive cancers from representative GEMM and xenograft mice are shown in Figure 2. The MIN lesions in C3(1) mice arise *de novo* within an intact mammary fat pad, surrounded by normal tissue. Conversely, DCIS arising in MCF10DCIS mice appears as larger palpable lesions that are not embedded within an intact mammary gland. Given that the imaging presentation of human DCIS is more akin to the GEMM, i.e., a typically nonpalpable lesion embedded in the normal breast, the remainder of our analysis was focused on MIN lesions in C3(1) SV40 Tag mice.

A total of 60 MIN lesions were histologically confirmed, of which MRI detected 53 for an overall sensitivity of 88% (53/60). The sensitivity of MRI was higher in the posterior inguinal glands compared to the anterior inguinal glands, although this difference was not statistically significant ( $p > 0.2$ ). Similarly, the sensitivity of MRI-directed ultrasound was significantly higher in the posterior glands, at 97%, compared to the anterior inguinal glands, at 37% ( $p < 0.0001$ ) (Table 1).

Qualitative analysis (Table 2) of lesion morphology according to the mBIRADS lexicon revealed that the predominant distribution of nonmass MIN lesions was segmental, with a homogeneous pattern. Quantitatively (Figure 3), MIN lesions presented with a significantly higher SNR than NMG on T<sub>1</sub> FFE (at  $35 \pm 7$  vs.  $18 \pm 2$ , respectively) and T<sub>2</sub> TSE (at  $29 \pm 8$  vs.  $13 \pm 3$ , respectively) ( $p < 0.0001$ ), and a significantly lower SNR compared to lymph nodes and invasive tumors ( $p < 0.001$ ). Although MIN lesions exhibited higher SNR on T<sub>1</sub> FFE than on T<sub>2</sub> TSE ( $p < 0.0002$ ), both MIN and invasive tumors achieved comparable CNR<sub>NMG</sub> on T<sub>1</sub> and T<sub>2</sub> weighted acquisitions ( $p > 0.2$ ) and significantly higher CNR<sub>muscle</sub> on T<sub>2</sub> TSE ( $p < 0.0001$ ). DCEMRI was obtained for 15/53 MRI-detected MIN lesions. Analysis of kinetic curve shape demonstrated that 20% (3/15) exhibited minimal enhancement, while 47% (7/15) displayed a plateau curve shape and 20% (3/15) a washout curve shape. For the  $n=12$  enhancing MIN, the average  $K^{\text{trans}}$  and  $v_e$  values were  $0.11 \pm 0.09 \text{ min}^{-1}$  and  $0.47 \pm 0.22$ , respectively.

## DISCUSSION

Our results suggest that from an imaging perspective the C3(1) SV40 Tag GEMM more faithfully mimics human DCIS compared to the commonly used MCF10DCIS xenograft model. In GEMMs, preinvasive cancers arise stochastically within pre-existing mammary ducts and are surrounded by the mammary gland microenvironment including an intact immune system. Although intramammary fat pad injections of MCF10DCIS cells did not achieve this phenotype, recently developed xenograft models may do so. For example, DCIS patient-derived cells that are injected directly into the murine ductal system via the nipple may prove to be more effective models of DCIS (Valdez et al., 2011, Behbod et al., 2009).

Previous studies have shown that on small bore small animal imaging systems at high magnetic field strength (4.7 T and 9.4 T), it is possible to detect preinvasive cancers in transgenic mice using a proton density/moderately  $T_1$  weighted pulse sequence (Gradient Recalled Echo, TR/TE ~1000/5.5 ms) (Jansen et al., 2008, Jansen et al., 2011). Our study complements this prior work in several important ways. We have implemented pulse sequences that are more similar to clinically acquired  $T_1$  and  $T_2$  weighted breast MRI, on a 3T clinical MRI scanner. In doing so, we have established a new  $T_1$  weighted fast-field echo imaging approach for preinvasive murine neoplasias that matches or exceeds the sensitivity, SNR and  $CNR_{\text{NMG}}$  of prior techniques, in half the imaging time. Finally, we found that the  $CNR_{\text{NMG}}$  of preinvasive neoplasia on  $T_2$  TSE was comparable to  $T_1$  FFE, whereas in prior studies  $T_2$  weighting was not reported to be as effective (Jansen et al., 2008).

Human DCIS is typically detected with  $T_1$  FFE after the administration of a gadolinium-chelated based contrast agent (Kuhl et al., 2007). Conversely, we have found that murine MIN can be visualized on  $T_1$  FFE and  $T_2$  TSE with high  $CNR_{\text{NMG}}$  without contrast medium. The mechanisms responsible for this important discrepancy are not clear. Given the likelihood that the magnetic properties of neoplastic epithelial cells/ducts may be similar in mice and women at 3T, it may be differences in the tumor microenvironment that yield a different imaging phenotype. For example, neoplastic ducts in the mouse are distributed sparsely within a fat pad, whereas in women they may be in close proximity with normal TDLUs embedded within an intralobular stroma. In performing a contrast kinetic characterization of

MIN lesions at 3T we found some qualitative and quantitative similarities with human disease, including exhibiting a predominantly plateau or washout curve shape (Jansen et al., 2007) and comparable values of  $K^{\text{trans}}$  and  $v_e$  (Furman-Haran et al., 2005). However, our DCEMRI methods were limited and further improvements are required, including increased population size and temporal resolution, to better compare the contrast enhanced phenotype of murine and human preinvasive neoplasias.

Molecular and metabolic imaging is highly desirable to better reveal biological diversity in mouse models of DCIS. Indeed, in previous work by Abbey et al, FDG-PET imaging was used to characterize metabolic changes during breast cancer progression in an allograft mouse model of DCIS (Abbey et al., 2004, Abbey et al., 2006). However, molecular imaging techniques often suffer from poor spatial resolution and anatomic localization, and could thus benefit from concomitant anatomic imaging for lesion detection and localization. Our results set the stage for such an approach, as we have established rapid, high resolution and highly sensitive anatomic imaging techniques in two different modalities, MRI and ultrasound. Furthermore, in carefully mapping out the lesions in this study, we found improved sensitivity in the posterior inguinal glands compared to anterior inguinal glands, likely due to partial volume effects near the belly of the mouse.

For multimodality imaging it is also essential to develop co-registration methods that can accurately correlate diverse images with one another other and with histology. This is particularly relevant for small preinvasive mammary cancers that are not palpable or visible. Prior work in MRI-ultrasound correlation has been developed for palpable lesions. For example Loveless et al. developed an iterative closest point algorithm method to co-register MRI and ultrasound images using palpable tumors ( $\sim 100\text{mm}^3$ ) arising in a xenograft model of breast cancer (Loveless et al., 2009). The novel approach we have established in this study utilizes the agar grid as a two dimensional coordinate system that can accurately co-register *in vivo* images and histology of sub-millimeter cancers.

Ultimately we are interested in investigating the capacity for image-based biomarkers to identify molecular or prognostic subtypes of human DCIS, using GEMMs as a model system. In this study, we have added to the imaging toolkit that can be used to characterize murine preinvasive neoplasia by

developing new clinically relevant MRI techniques at 3 Tesla, adding ultrasound characterization and establishing a new multi-modality correlation strategy. In future work, application of more advanced imaging techniques, such as diffusion weighted MRI and contrast enhanced ultrasound, can yield additional quantitative measures of lesion biology and physiology. However, in addition to improved imaging techniques it is also essential to utilize more diverse GEMMs of DCIS. Imaging investigations of murine MIN have been limited to models wherein viral proteins (e.g., SV40 Tag (Jansen et al., 2008, Jansen et al., 2011, Jansen et al., 2009b) and PyMT (Abbey et al., 2006, Namba et al., 2006, Abbey et al., 2004)) induce aggressive tumorigenesis by concurrently altering several molecular pathways (Green et al., 2000). However, these models do not capture the full complexity of human DCIS. More advanced GEMMs can target individual pathways known to be altered in DCIS, including Rb (Simin et al., 2004), HER2 (Moody et al., 2002) and PTEN (Dourdin et al., 2008) in a cell type and temporally controlled manner. It is by combining advanced imaging approaches with sophisticated mouse modeling techniques that insights on image-based biomarkers of DCIS are likely to follow.



## **ACKNOWLEDGEMENTS**

We thank Dr. Esta Sterneck for use of the C3(1) SV40 Tag mice, Dr. Peter Choyke for useful discussions and comments on the manuscript, and Dr. Yuxi Pang for assistance with the DCEMRI analysis software.

This project has been funded in part with federal funds from the National Cancer Institute, National Institutes of Health, under Contract No. HHSN261200800001E.

The content of this publication does not necessarily reflect the views of policies of the Department of Health and Human Services, nor does mention of trade names, commercial products, or organizations imply endorsement by the U.S. Government.

**TABLES****Table 1:** Sensitivity of MRI and MRI-directed ultrasound for MIN in different gland regions of C3(1) SV40 Tag mice.

	<b>Number of MIN histologically</b>	<b>Sensitivity of MRI</b>	<b>Sensitivity of MRI- directed ultrasound</b>
<b>All inguinal glands</b>	60	88% (53/60)	72% (38/53)
<b>Posterior inguinal glands</b>	33	94% (31/33)	97% (30/31)
<b>Anterior inguinal glands</b>	27	82% (22/27)	36%(8/22)

**Table 2:** Qualitative mBIRADS features for MIN lesions in C3(1) SV40 Tag mice.

		<b>MIN</b>
		<b>No. (%)</b>
<b>Type</b>	Mass	0 (0)
	Nonmass	53 (100)
<b>Distribution</b>	Linear	15 (28)
	Ductal	11 (21)
	Segmental	27 (51)
<b>Pattern</b>	Homogeneous	23 (43)
	Stippled	20 (38)
	Clumped	10 (19)

## FIGURE CAPTIONS

**Figure 1.** Multimodality imaging workflow. **A.** Initially, the agar grid is wrapped around the mouse and grid edge positions marked on the skin of the mouse. **B.** MRI of one axial cross-section through the mouse (dotted line from A) revealing an intramammary lymph node (red arrow). The agar grid can be seen on MRI (arrows) and thus the grid coordinates of the lymph node noted. **C.** After removing the mouse from the imaging coil, the location of the MRI detected lesion is marked on the skin of the mouse to guide placement of the ultrasound transducer. **D.** Ultrasound imaging is performed to locate and evaluate the MRI-detected lesion. **E.** Finally, the animal is euthanized and glands are excised for histological analysis. Shown are the posterior inguinal glands #4 and 9 (outlined in blue), the anterior inguinal glands #5 and #10 (outlined in black) and the intramammary lymph nodes circled in orange.

**Figure 2.** Representative noncontrast  $T_1$  FFE,  $T_2$  TSE, ultrasound and H&E images from a normal gland (top row), MIN lesion in the C3(1) SV40 Tag GEMM (middle row, thin arrows) and DCIS lesion in the MCF10DCIS xenograft model (bottom row, thin arrows). Intramammary lymph nodes are identified by arrowheads, while an invasive tumor (middle row) is indicated with a gray arrow.

**Figure 3.** The SNR,  $CNR_{NMG}$  and  $CNR_{muscle}$  of lymph nodes, MIN and invasive tumors in C3(1) SV40 Tag mice on noncontrast  $T_1$  FFE and  $T_2$  TSE acquisitions.

**Figure 1.** Example multimodality imaging workflow. **A.** Initially, the agar grid is wrapped around the mouse and grid edge positions marked on the skin of the mouse. **B.** MRI of one axial cross-section through the mouse (dotted line from A) revealing an intramammary lymph node (red arrow). Because the agar grid is MR-visible, the grid coordinates of the lymph node are noted. **C.** After removing the mouse from the imaging coil, the location of the MRI detected lesion is marked on the skin of the mouse to guide placement of the ultrasound transducer. **D.** Ultrasound imaging is performed to locate and evaluate the MRI-detected lesion. **E.** Finally, the animal is euthanized and glands are excised for histological analysis. Shown are the posterior inguinal glands #4 and 9 (outlined in blue), the anterior inguinal glands #5 and #10 (outlined in black) and the intramammary lymph nodes circled in white.

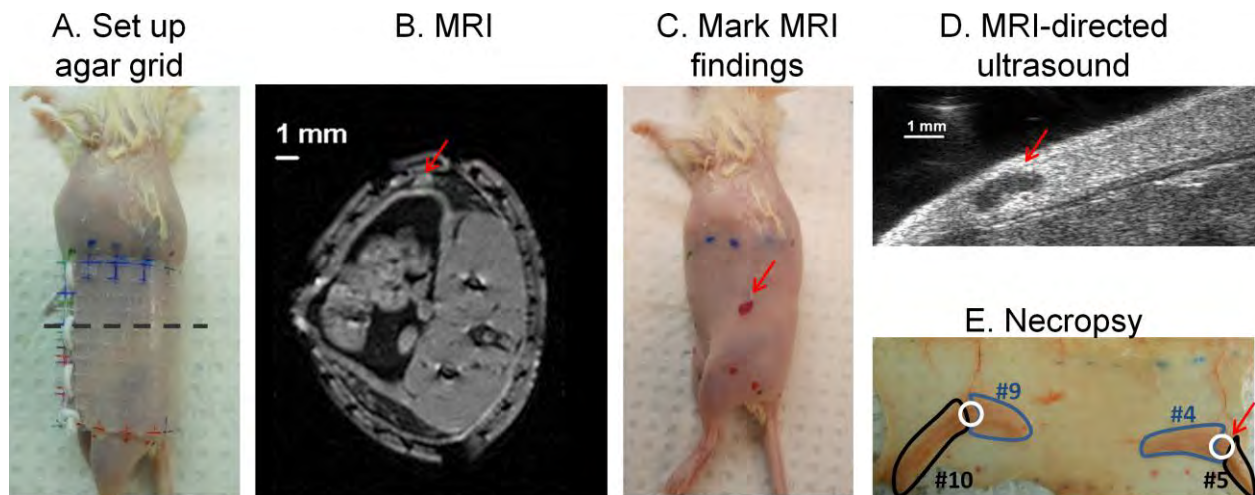


**Figure 2.** Representative noncontrast T<sub>1</sub> FFE, T<sub>2</sub> TSE, ultrasound and H&E images from a normal gland (top row), MIN lesion in the C3(1) SV40 Tag GEMM (middle row, thin arrows) and DCIS lesion in the MCF10DCIS xenograft model (bottom row, thin arrows). Intramammary lymph nodes are identified by arrowheads.

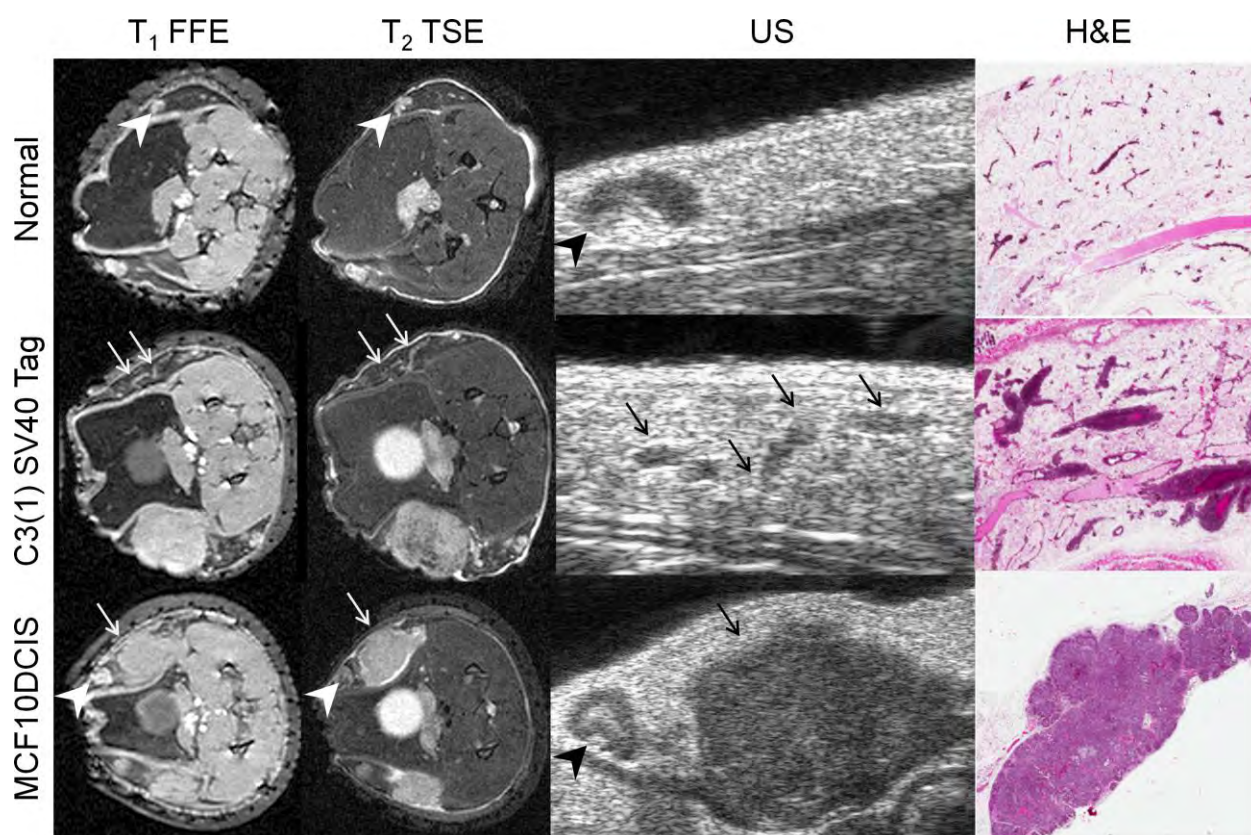
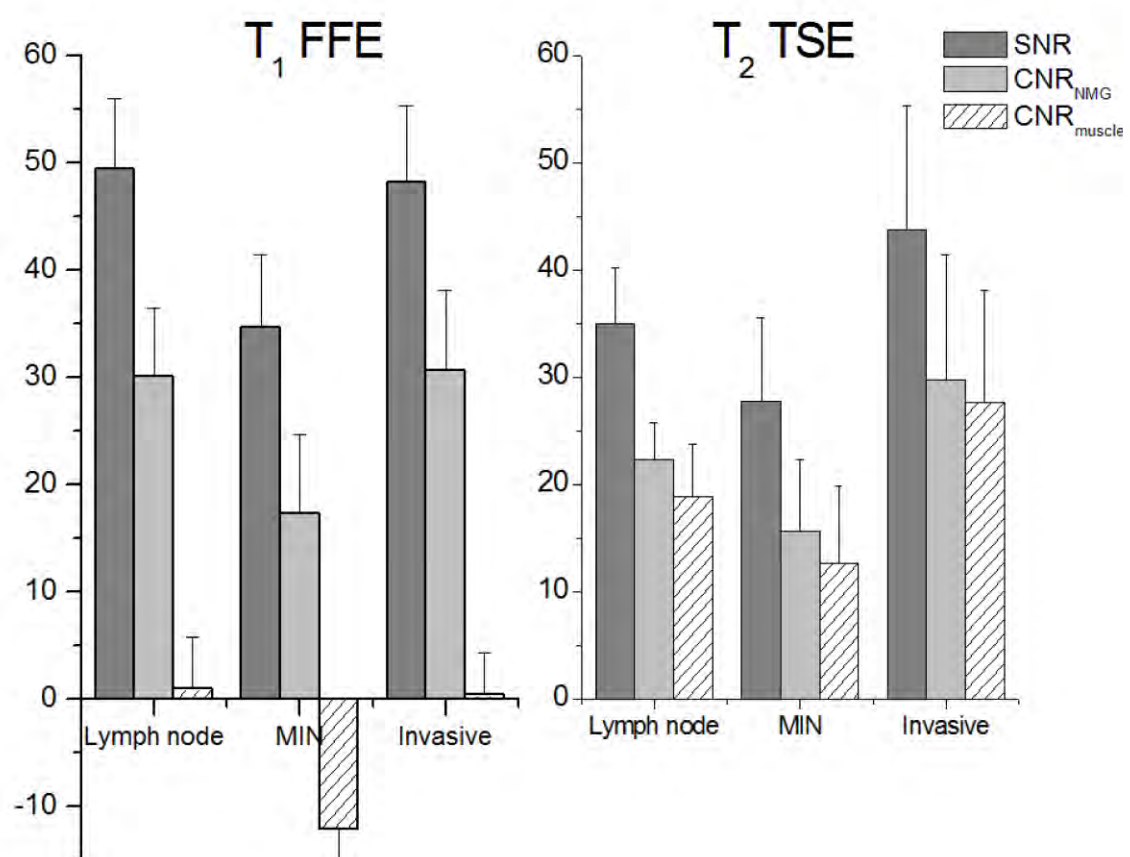




**Figure 3.** The SNR,  $CNR_{NMG}$  and  $CNR_{muscle}$  of lymph nodes, MIN and invasive tumors in C3(1) SV40 Tag mice on  $T_1$  FFE and  $T_2$  TSE acquisitions.



## REFERENCES

- Abbey C K, Borowsky A D, Gregg J P, Cardiff R D and Cherry S R 2006 Preclinical imaging of mammary intraepithelial neoplasia with positron emission tomography *Journal of mammary gland biology and neoplasia* **11** 137-49.
- Abbey C K, Borowsky A D, Mcgoldrick E T, Gregg J P, Maglione J E, Cardiff R D and Cherry S R 2004 In vivo positron-emission tomography imaging of progression and transformation in a mouse model of mammary neoplasia *Proceedings of the National Academy of Sciences of the United States of America* **101** 11438-43.
- Abe H, Schmidt R A, Shah R N, Shimauchi A, Kulkarni K, Sennett C A and Newstead G M 2010 MR-directed ("Second-Look") ultrasound examination for breast lesions detected initially on MRI: MR and sonographic findings *AJR. American journal of roentgenology* **194** 370-7.
- ACR 2003. *American College of Radiology: ACR Breast Imaging Reporting and Data System Atlas (BI-RADS)*. Reston, VA.
- Allegra C J, Aberle D R, Ganschow P, Hahn S M, Lee C N, Millon-Underwood S, Pike M C, Reed S D, Saftlas A F, Scarvalone S A, Schwartz A M, Slomski C, Yothers G and Zon R 2010 National Institutes of Health State-of-the-Science Conference statement: Diagnosis and Management of Ductal Carcinoma In Situ September 22-24, 2009 *Journal of the National Cancer Institute* **102** 161-9.
- Allred D C 2010 Ductal carcinoma in situ: terminology, classification, and natural history *Journal of the National Cancer Institute. Monographs* **2010** 134-8.
- Behbod F, Kittrell F S, Lamarca H, Edwards D, Kerbawy S, Heestand J C, Young E, Mukhopadhyay P, Yeh H W, Allred D C, Hu M, Polyak K, Rosen J M and Medina D 2009 An intraductal human-in-mouse transplantation model mimics the subtypes of ductal carcinoma in situ *Breast cancer research : BCR* **11** R66.
- Cho N, Moon W K, Chang J M, Yi A, Koo H R, Park J S and Park I A 2011 Sonoelastographic lesion stiffness: preoperative predictor of the presence of an invasive focus in nonpalpable DCIS diagnosed at US-guided needle biopsy *European radiology* **21** 1618-27.
- D'orsi C J 2010 Imaging for the diagnosis and management of ductal carcinoma in situ *Journal of the National Cancer Institute. Monographs* **2010** 214-7.
- Dourdin N, Schade B, Lesurf R, Hallett M, Munn R J, Cardiff R D and Muller W J 2008 Phosphatase and tensin homologue deleted on chromosome 10 deficiency accelerates tumor induction in a mouse model of ErbB-2 mammary tumorigenesis *Cancer research* **68** 2122-31.
- Erbas B, Provenzano E, Armes J and Gertig D 2006 The natural history of ductal carcinoma in situ of the breast: a review *Breast cancer research and treatment* **97** 135-44.
- Furman-Haran E, Schechtman E, Kelcz F, Kirshenbaum K and Degani H 2005 Magnetic resonance imaging reveals functional diversity of the vasculature in benign and malignant breast lesions *Cancer* **104** 708-18.
- Green J E, Shibata M A, Yoshidome K, Liu M L, Jorcyk C, Anver M R, Wigginton J, Wiltrout R, Shibata E, Kaczmarczyk S, Wang W, Liu Z Y, Calvo A and Couldrey C 2000 The C3(1)/SV40 T-antigen transgenic mouse model of mammary cancer: ductal epithelial cell targeting with multistage progression to carcinoma *Oncogene* **19** 1020-7.
- Hu M, Yao J, Carroll D K, Weremowicz S, Chen H, Carrasco D, Richardson A, Violette S, Nikolskaya T, Nikolsky Y, Bauerlein E L, Hahn W C, Gelman R S, Allred C, Bissell M J, Schnitt S and Polyak K 2008 Regulation of in situ to invasive breast carcinoma transition *Cancer cell* **13** 394-406.
- Jansen S A 2011 Ductal carcinoma in situ: detection, diagnosis, and characterization with magnetic resonance imaging *Semin Ultrasound CT MR* **32** 306-18.
- Jansen S A, Conzen S D, Fan X, Krausz T, Zamora M, Foxley S, River J, Newstead G M and Karczmar G S 2008 Detection of in situ mammary cancer in a transgenic mouse model: in vitro and in vivo

- MRI studies demonstrate histopathologic correlation *Physics in medicine and biology* **53** 5481-93.
- Jansen S A, Conzen S D, Fan X, Markiewicz E, Krausz T, Newstead G M and Karczmar G S 2011 In vivo MRI of early stage mammary cancers and the normal mouse mammary gland *NMR in biomedicine* **24** 880-7.
- Jansen S A, Conzen S D, Fan X, Markiewicz E J, Newstead G M and Karczmar G S 2009a Magnetic resonance imaging of the natural history of in situ mammary neoplasia in transgenic mice: a pilot study *Breast cancer research : BCR* **11** R65.
- Jansen S A, Newstead G M, Abe H, Shimauchi A, Schmidt R A and Karczmar G S 2007 Pure ductal carcinoma in situ: kinetic and morphologic MR characteristics compared with mammographic appearance and nuclear grade *Radiology* **245** 684-91.
- Jansen S A, Paunesku T, Fan X, Woloschak G E, Vogt S, Conzen S D, Krausz T, Newstead G M and Karczmar G S 2009b Ductal carcinoma in situ: X-ray fluorescence microscopy and dynamic contrast-enhanced MR imaging reveals gadolinium uptake within neoplastic mammary ducts in a murine model *Radiology* **253** 399-406.
- Kerlikowske K 2010 Epidemiology of ductal carcinoma in situ *Journal of the National Cancer Institute. Monographs* **2010** 139-41.
- Kuhl C K, Schrading S, Bieling H B, Wardelmann E, Leutner C C, Koenig R, Kuhn W and Schild H H 2007 MRI for diagnosis of pure ductal carcinoma in situ: a prospective observational study *Lancet* **370** 485-92.
- Lari S A and Kuerer H M 2011 Biological Markers in DCIS and Risk of Breast Recurrence: A Systematic Review *Journal of Cancer* **2** 232-61.
- Loveless M E, Whisenant J G, Wilson K, Lyschik A, Sinha T K, Gore J C and Yankeelov T E 2009 Coregistration of ultrasonography and magnetic resonance imaging with a preliminary investigation of the spatial colocalization of vascular endothelial growth factor receptor 2 expression and tumor perfusion in a murine tumor model *Molecular imaging* **8** 187-98.
- Maroulakou I G, Anver M, Garrett L and Green J E 1994 Prostate and mammary adenocarcinoma in transgenic mice carrying a rat C3(1) simian virus 40 large tumor antigen fusion gene *Proceedings of the National Academy of Sciences of the United States of America* **91** 11236-40.
- Miller F R, Santner S J, Tait L and Dawson P J 2000 MCF10DCIS.com xenograft model of human comedo ductal carcinoma in situ *Journal of the National Cancer Institute* **92** 1185-6.
- Moody S E, Sarkisian C J, Hahn K T, Gunther E J, Pickup S, Dugan K D, Innocent N, Cardiff R D, Schnall M D and Chodosh L A 2002 Conditional activation of Neu in the mammary epithelium of transgenic mice results in reversible pulmonary metastasis *Cancer cell* **2** 451-61.
- Namba R, Young L J, Abbey C K, Kim L, Damonte P, Borowsky A D, Qi J, Tepper C G, Macleod C L, Cardiff R D and Gregg J P 2006 Rapamycin inhibits growth of premalignant and malignant mammary lesions in a mouse model of ductal carcinoma in situ *Clinical cancer research : an official journal of the American Association for Cancer Research* **12** 2613-21.
- Simin K, Wu H, Lu L, Pinkel D, Albertson D, Cardiff R D and Van Dyke T 2004 pRb inactivation in mammary cells reveals common mechanisms for tumor initiation and progression in divergent epithelia *PLoS biology* **2** E22.
- Turkbey B, Pinto P A, Mani H, Bernardo M, Pang Y, McKinney Y L, Khurana K, Ravizzini G C, Albert P S, Merino M J and Choyke P L 2010 Prostate cancer: value of multiparametric MR imaging at 3 T for detection--histopathologic correlation *Radiology* **255** 89-99.
- Valdez K E, Fan F, Smith W, Allred D C, Medina D and Behbod F 2011 Human primary ductal carcinoma in situ (DCIS) subtype-specific pathology is preserved in a mouse intraductal (MIND) xenograft model *The Journal of pathology* **225** 565-73.
- Van Dyke T and Jacks T 2002 Cancer modeling in the modern era: progress and challenges *Cell* **108** 135-44.